TECHNICAL MEMORANDUM

362

Potential improvement of forecasts of two severe storms using targeted observations

M. Leutbecher[1,2], J. Barkmeijer[2], T. N. Palmer[2] and A. J. Thorpe[3]

Research Department

[1] Météo-France/CNRM
[2] ECMWF
[3] NERC Centres for Atmospheric Science, Dept. of Meteorology, University of Reading

(accepted for publication in Q. J. R. Meteorol. Soc.)

March 2002

European Centre for Medium-Range Weather Forecasts
Europäisches Zentrum für mittelfristige Wettervorhersage
Centre européen pour les prévisions météorologiques à moyen terme

For additional copies please contact

The Library
ECMWF
Shinfield Park
Reading
RG2 9AX
library@ecmwf.int

Series: ECMWF Technical Memoranda

A full list of ECMWF Publications can be found on our web site under:
http://www.ecmwf.int/pressroom/publications/

Summary

The potential to improve short-range forecasts of two extra-tropical storms by using supplementary observations in regions lacking accurate observations is investigated. In the idealized framework used here, a control and a truth experiment are selected from a set of forecasts initialized with analyses from different NWP centres. Synthetic soundings of wind and temperature are created from the truth experiment and are assimilated with 4DVAR using the operational observation error estimates for radiosondes and the initial condition of the control experiment as background. Through multiple analysis/forecast experiments we obtain a nonlinear estimate of the optimal zone for observing (OZO); that is the zone in which the use of a given number of supplementary observations leads to the largest reduction in forecast error. We evaluate targeting techniques based on either total energy singular vectors (TESVs) or on Hessian singular vectors (HSVs) by comparison with the OZO and by comparison with experiments in which the same amount of supplementary observations is distributed in an un-targeted manner, namely with a random distribution scheme (RDS).

Overall, the HSV targeting is superior to the TESV targeting in the two cases. In one case there is a significant difference between the target regions determined with TESVs and HSVs. The HSV based observing strategy resembles the OZO in terms of the observing region and the achieved forecast error reduction. With the RDS, the forecast error is variable and likely to be larger than the forecast error obtained with singular vector targeting. Experiments with target regions of different sizes show that supplementary observations in an area of about 3×10^6 km^2 are required to achieve a significant forecast improvement. A two-dimensional sampling pattern with soundings spaced at a distance of about 1–2 times the horizontal correlation length scale of the background error estimate appears very efficient. In additional impact experiments for one case, observations were perturbed with noise to represent observational error. The perturbations are almost as likely to improve the forecast as to worsen it compared to the forecast using unperturbed observations.

1 Introduction

Observations that are useful for NWP are distributed very inhomogeneously over the globe. Over the oceans and remote areas sufficiently accurate observations of wind and temperature are lacking. These regions will be referred to as poorly observed for short. Consequently, the initial condition error is not constrained enough to avoid poor forecasts even in the short range of 1–3 days. Adaptive observations have been proposed as an efficient way of reducing the frequency of poor forecasts caused by inaccurate initial conditions (Snyder 1996). The objective is to select sites for supplementary observations to improve the forecast in a specific region and at a specific future time. We will refer to these as the verification region and verification time, respectively. Promising sites for supplementary observations will be located in the region in which initial condition error is likely to contribute most to the forecast error. This region will be referred to as the sensitive region and it is our a priori estimate of the target region for the supplementary observations. It is not necessarily one connected domain. The optimal observing sites are those sites where the use of a set of additional observations actually reduces the forecast error the most. For a decision prior to the observing time, optimality needs to be defined in a statistical sense. Sites are sought at which additional observations are expected to reduce the forecast error the most. The expectation value has to be based on information available before the time when the observations are taken. Berliner *et al.* (1999) pose the problem of finding the statistically optimal sites rigorously for linear dynamics and normally distributed errors. Due to the dimension of the state space of NWP models only approximate solutions to this optimization problem are feasible.

A number of feasible techniques have been proposed. Adjoint sensitivities (Langland and Rohaly 1996), singular vectors (Palmer *et al.* 1998), quasi-inverse linear integrations (Pu *et al.* 1997) use a tangent-linear and/or adjoint of the forecast model to identify the target regions. The properties of the assimilation scheme can be taken into account by extending the sensitivity into observation space (Baker and Daley 2000; Doerenbecher and Bergot 2001). In the ensemble transform technique (Bishop and Toth 1999) and the ensemble transform Kalman filter (Bishop *et al.* 2001) an ensemble of possibly nonlinear trajectories is diagnosed assuming that the relevant perturbations evolve linearly. All techniques mentioned so far require that a linearization about

a control trajectory or ensemble mean trajectory is a useful description of the growth of initial errors into the dominant forecast errors (Hansen and Smith 2000). Tests of the techniques in field experiments have focussed on a forecast range of around 2 days. In this range, tangent-linear dynamics may be still a useful description of the evolving initial condition errors. Another observing strategy that does not depend on the usefulness of linear dynamics is to select locations where the uncertainty of the initial conditions is large or where additional observations are expected to reduce the initial error the most (Lorenz and Emanuel 1998; Hamill and Snyder 2002). These latter techniques are not optimal for improving the forecast as future error growth is not taken into account — in particular if the goal is to improve the forecast in a specific region.

Observations have been targeted in recent field experiments, such as FASTEX, NORPEX, and WSRP using ensemble techniques, adjoint sensitivities or singular vectors. The impact of these targeted observations on the forecast has been studied extensively (e.g. Bergot 2001; Langland *et al.* 1999; Szunyogh *et al.* 2000). In the majority of cases the forecast is improved in the verification region by using the targeted observations. This likely improvement may be questioned as proof of concept as any distribution of sufficiently accurate additional observations in an otherwise poorly observed region is likely to improve the forecast. The coverage of supplementary soundings taken in past field experiments is insufficient to compare the impact of a targeted distribution of soundings with the impact of an un-targeted distribution. This issue is addressed by Morss *et al.* (2001) in observing system simulation experiments with a quasi-geostrophic channel model. They compare ensemble spread targeting with randomly selecting observing sites. A further step in the evaluation of targeting strategies, which is feasible in observing system simulation experiments but not with the data from past field experiments, is to identify the optimal observing sites and thus the maximum reduction in forecast error that can be achieved with a given number of supplementary observations. Hansen and Smith (2000) determined the optimal site for a supplementary observation that reduces the forecast error the most in experiments with the 40-variable Lorenz '95 model. Reynolds *et al.* (2000) performed similar experiments with a 3-layer T21 quasi-geostrophic model. In their study, the effect of assimilating a set of supplementary observations is simulated by setting the initial error to zero in a disc. The optimal position of the disc is determined through multiple forecasts.

This study will make a comprehensive evaluation of observation targeting for two cases of severe extra-tropical storms that were poorly forecasted: the storm crossing Denmark on 3 December 1999 and the storm hitting France and neighbouring countries on 26 December 1999. We will call these the *Danish storm* and the *(first) French storm*, respectively. Observing system simulation experiments are performed with a realistic NWP model and its 4DVAR assimilation scheme. A perfect model scenario is employed, that is, the models for the simulation of the true state and for the forecast are the same. The impact is evaluated for observations targeted with total energy singular vectors (TESVs) and also for Hessian singular vectors (HSVs). The latter are calculated with an initial time norm based on the Hessian of the 4DVAR cost function which provides an estimate of the analysis error covariances. For observation targeting, the norm defined with the inverse of the analysis error covariances is the appropriate choice as structures with equal amplitude represent equally likely initial errors, given that the analysis error is normally distributed (Barkmeijer *et al.* 1998; Palmer *et al.* 1998). The test of HSVs for observation targeting in a realistic NWP context is novel. The singular vector targeting is compared with two types of benchmark experiments. We determine the impact of supplementary observations distributed randomly to estimate the typical impact of un-targeted upgrades of the observational network. We demand from an acceptable targeting technique that it beats this random distribution scheme (RDS) for most realizations of random sites. Furthermore, we estimate through multiple analysis-forecast experiments the zone in which the addition of a given number of supplementary observations leads to the largest reduction in forecast error. This optimal zone for observing (OZO) is a nonlinear estimate of the true optimal position for the supplementary observing sites. We will answer whether the singular vectors point close to the OZO and whether the observations targeted using singular vectors achieve an appreciable fraction of the forecast error reduction using the same amount of observations in the OZO.

Another objective of this work is to assess how the impact depends on the size of the target region and the spatial density of the supplementary observations. This aspect is a continuation of the type of work begun by Bergot *et al.* (1999). Finally, we investigate how the forecast error is affected by observational error of the supplementary observations. The improvement of the forecasts due to different distributions of additional observations is judged subjectively with sea-level pressure maps and objectively with a r.m.s. error measure integrated over the verification region.

The outline of the paper is as follows. In section 2 the method is described. In sections 3 and 4 the impact studies for the different strategies to distribute 40 soundings are presented for the first French storm and the Danish storm, respectively. Section 5 contains additional impact studies with differently sized target regions and with a lower sampling density. The effect of observational error on the forecast skill is discussed in section 6. Section 7 contains a discussion of the results.

2 Methodology

2.1 Observing System Simulation Experiment

The impact of the supplementary observations is tested in a perfect model scenario. First a "truth" and a "control" trajectory are selected from an ensemble of forecasts. Second, "synthetic" observations are constructed from the truth experiment. Each observing strategy corresponds to a distinct set of observations. Third, a new analysis and forecast are computed for each set of observations.

Here, truth and control are chosen from a multi-analyses ensemble (Richardson 2001). The ensemble consists of four forecasts that start from the analyses of the German Weather Service (DWD), the European Centre for Medium-Range Weather Forecasts (ECMWF), Météo-France (MF), and the UK Meteorological Office (UKMO). The integrations are performed with the IFS model of ECMWF at a resolution of T_L255 in the horizontal and 31 levels in the vertical (model cycle 21r4). The ensemble members are compared with the actual evolution of the system of interest and subjectively ranked. A poor forecast is chosen as the control and the best forecast is chosen as truth.

The supplementary observations are treated as in situ measurements of wind and temperature from dropsondes or radiosondes. The data are interpolated from the initial condition fields of the truth experiment. The soundings consist of observations at the 22 model levels between the surface and 200 hPa. The distribution of real adaptive observations in time and space will depend on the observing platform available. We decided to keep this work independent of particular platform dependent choices. An idealized scenario is considered in which the supplementary soundings are simultaneous and are distributed either at a constant spatial density or at randomly selected sites. The first set of impact experiments discussed in sections 3–5 uses perfect observations. Thus the interpretation of individual experiments is meaningful as the impact does not depend on the actual realization of the observational error. In section 6, the effect of observational error on forecast error is studied. This is done with a small ensemble with individual members differing only by the random numbers used to perturb the observations.

As only the adaptive part of the observing network is simulated, the assimilation method has to differ from the operational scheme, in which all observations and the background fields determine the analysis. Here, the analysis is obtained in two steps. The first step is the assimilation that leads to the analysis of the control experiment. This analysis contains the information from a first guess and the conventional observing network. This analysis is then used as new first guess in a subsequent assimilation which is provided only with the synthetic observations.

The synthetic observations are assimilated with 4DVAR over a 6-hour period. The observation time of the synthetic observations is in the middle of the assimilation period. The scheme uses the incremental approach (Courtier *et al.* 1994). The nonlinear trajectory is updated once during the minimization. The increments have a horizontal resolution of T63. The background error correlations are derived from an ensemble of analyses. The synthetic observations are assimilated using the operational observation error estimate for radiosondes. Thus, the assimilation scheme is not aware of the fact that the observations happen to have zero error in some of the experiments. We decided to use the computationally demanding 4DVAR scheme instead of 3DVAR in order to use a system that would be also well suited for the assimilation of targeted observations which are distributed in time. In the idealized experiments discussed here, we expect a small benefit from using 4DVAR due to the implicit 3-hour evolution of the background error correlations.

2.2 Singular Vector based Target Regions

Singular vectors optimized for total energy in the verification region are employed to identify the sensitive regions of the atmosphere, where initial condition error is likely to contribute most to the forecast error. The initial time t_i of the optimization period is the targeting time, that is the time when the adaptive observations are taken. The final time t_f of the optimization period is the verification time. Here, $t_f - t_i = 48$ h.

Singular vectors depend on norms that are used to measure their amplitude at initial and final time. For predictability studies, the analysis error covariance norm is the appropriate norm at initial time as it accounts for the pdf of the initial error (Palmer *et al.* 1998). This norm is defined by $\|\mathbf{x}\|_a^2 = \mathbf{x}^t \mathbf{A}^{-1} \mathbf{x}$, where $\mathbf{A}$ is the covariance of initial error associated with the conventional observing network. The variational assimilation scheme provides an estimate of the analysis error covariance via the Hessian of the cost function $\mathbf{A}^{-1} = \nabla\nabla J$ (Rabier and Courtier 1992). Therefore, the optimal structures computed with this initial time norm are called Hessian singular vectors (HSVs). Barkmeijer *et al.* (1998) describe their computation via a generalized Davidson algorithm and present results obtained with a 5 layer T21 primitive-equation model using the Hessian of the 3DVAR cost function for the initial time norm. Barkmeijer *et al.* (1999) extend this work to higher spatial resolution and compare the properties of TESVs and HSVs in the context of ensemble forecasting. In our study, HSVs are computed using the cost function of a 6-hour 4DVAR assimilation of the conventional observations.

The use of HSVs for targeting is novel. Previously, so called total energy singular vectors (TESVs) were used. They are cheaper to compute than HSVs as the initial time norm based on total energy is diagonal. The total energy norm is given by:

$$\|\mathbf{x}\|_e^2 = \mathbf{x}^t \mathbf{E} \mathbf{x} = \frac{1}{2} \int_{p_0}^{p_1} \int_S (u^2 + v^2 + \frac{c_p}{T_r} T^2) \, dp \, ds + \frac{1}{2} R_d T_r p_r \int_S (\ln p_{\mathrm{sfc}})^2 \, ds, \tag{1}$$

where $u, v, T, p_{\mathrm{sfc}}$ denote the zonal and meridional wind components, the temperature and the surface pressure of the state vector $\mathbf{x}$. Furthermore, c_p, R_d are the specific heat at constant pressure and the gas constant for dry air; $T_r = 300$ K and $p_r = 800$ hPa are reference values of temperature and pressure. The integration extends over the entire sphere S and all model levels. Let $\mathbf{E}$ denote the symmetric matrix that induces the total energy norm. Targets computed for both types of singular vectors will be compared.

The singular vectors are calculated as perturbations of the nonlinear control trajectory. In an operational setting the singular vectors need to be computed from a forecast initialized 1–2 days prior to the targeting time. Errors in the trajectory introduce some additional uncertainty about the target region (Buizza and Montani 1999; Gelaro *et al.* 1999). The sensitivity to the trajectory will be further addressed in section 7. The singular vectors are computed with a version of the tangent-linear and adjoint of the model which is adiabatic and frictionless apart from diffusion in the horizontal and vertical and surface drag. The resolution is T42 in the horizontal and 31 levels in the vertical.

The targeting of the additional observations can be viewed as a constrained optimization problem. Here, the constraint is formulated rather generally; other constraints that will depend on the observing platform are not considered. In an operational context, such additional constraints are certainly present and should be included in the optimization. Here, only the area of the target region and the spatial density of the sounding locations are specified. Thereby, the number of soundings is also prescribed. The target is not necessarily composed of just one connected region.

The singular vectors at initial time t_i define the regions in which a reduction of the initial uncertainty may increase the accuracy of the forecast at the verification time t_f and in the verification region the most. Because we imagine the supplementary observations are vertical soundings, the problem of finding optimal sounding sites is essentially one of finding a horizontal area. The sensitive region is diagnosed, following Montani *et al.* (1999), from the leading M singular vectors using a weighted average of the vertically integrated energy:

$$F(\lambda,\phi) = \sum_{j=1}^{M} \sigma_j e_j(\lambda,\phi). \tag{2}$$

Here λ,ϕ denote longitude and latitude and e_j the vertically integrated energy of singular vector j as given by the vertical integral of the wind and temperature perturbations in (1). Either TESVs or HSVs are used in (2). Both types of singular vectors are normalized to have unit total energy at initial time. The weight given to the contribution from singular vector j is its singular value σ_j in order to emphasize the structures that are likely to contribute most to the forecast error. The function F ranks geographical locations (λ,ϕ) according to the sensitivity of the forecast to errors of the initial condition at that location. The target region is defined as the set $D = \{(\lambda,\phi)|F(\lambda,\phi) > F_c\}$, in which F exceeds a threshold value F_c. The value of F_c is adjusted in order to obtain a target region with a pre-specified area a. The value of F_c for a given a is larger for targets computed with HSVs than for targets computed with TESVs, as the latter are spatially more confined and yield a larger maximum value of F. Here, the first five singular vectors are included in the computation of F as the target regions change only little if more singular vectors are taken into account.

2.3 Configurations of Observing Sites

The impact on the forecast is determined for several different configurations of observing sites: the singular vector based targeting strategies, the RDS, the OZO and a hemispheric network.

The OZO is the optimal zone for a given initial error taking into account the assimilation system and the nonlinear forecast model. There are several reasons why the singular vectors could fail to point to the OZO. First of all, the singular vector target is independent of the actual initial condition error and forecast errors. Implicitly, through the initial time norm the singular vector target depends on the assumed covariance of the analysis errors. Second, the tangent-linear and adjoint versions of the forecast model could be a poor approximation of the evolution of perturbations of the nonlinear forecast model. This could be due to the lack of spatial resolution and the lack of physical processes in the tangent-linear model and due to actual nonlinearities.

We choose to sample the target regions with soundings distributed at a constant spatial density. This sampling pattern is deemed to be superior to the arrangement of soundings along isolated flight tracks cutting through the target region. With new observing platforms like the driftsonde it may be possible to approximate this sampling strategy. The optimal spacing of the sounding locations depends on the properties of the assimilation scheme. The horizontal correlation length scale L of the background error provides an appropriate scale for the spacing Δs of the sounding locations. Redundant information will be collected if $\Delta s \ll L$, whereas data voids appear if $\Delta s \gg L$. In the assimilation scheme used in this study, the horizontal correlation length scales for surface pressure, vorticity, the unbalanced parts of divergence and temperature are about 400, 200, 200, and

Tab. 1: Overview of observing strategies. Spacing between soundings, number of soundings, and area sampled by soundings.

strategy	spacing (km)	number	area (10^6 km^2)
hemispheric	280	3393	261
TESV/HSV	280	160	12
TESV/HSV	560	40	12
TESV/HSV	280	40	3.1
TESV/HSV	560	10	3.1
TESV/HSV	280	10	0.9
RDS	≥ 560	40	67
OZO	280	40	3.1

300 km respectively. Therefore, spacings of 280 km and 560 km are used. These will be referred to as high and low spatial (observation) density. A constant spatial density on the sphere is achieved by using a constant latitudinal resolution of $\Delta\phi = \Delta s/111$ km and a variable longitudinal resolution of about $\Delta\phi/\cos\phi$, where ϕ denotes latitude. The low and high spatial density correspond to 2.5° and 5° latitudinal resolution. The smaller spacing is of the same order of magnitude as the T63 resolution of the analysis increments, which corresponds to a 200 km mesh size.

Experiments are performed with targets diagnosed from TESVs and from HSVs as already described. Target regions of three different sizes are considered: $0.9, 3, 12 \times 10^6$ km^2; these will be referred to as small, medium and large (singular vector) target. The small and medium targets are small enough so that they could be sampled with dropsondes deployed by one or two aircraft. Experiments were run for the three target sizes using the high observation density. This requires 10, 40 and 160 soundings to cover the targets of the various sizes. Additionally, the impact has been determined for the medium and the large target region using the low observation density, which requires 10 and 40 soundings, respectively (Table 1).

The impact from soundings in the singular vector targets is contrasted with the impact from soundings distributed over a large upstream region in an un-targeted manner using a random distribution scheme (RDS). To define an appropriate upstream region, we assume that the Atlantic sector (0°–90°W, 20°–65°N) and the polar region (65°–90°N) constitute the domain in which initial conditions mainly influence the two-day forecast over Europe in a zonal flow regime. Most of the upstream region lacks accurate observations. Experiments will be presented in which 40 soundings are scattered over this upstream region. The soundings are selected from a set of 219 locations that cover the upstream region at 560 km spacing (Fig. 1). An algorithm based on a random number generator picks 40 locations from the set of 219. The probability of being selected is $\frac{40}{219}$ for each location. The RDS is tested for five different initializations of the random number generator as we expect that the impact depends on the actual choice of locations. Clusters of soundings, which would provide redundant information, cannot occur as the imposed minimum distance between soundings is 560 km.

A crude upper bound on the maximum possible forecast improvement achievable with a limited set of targeted observations is obtained from an experiment in which the entire northern hemisphere is covered with 3393 soundings using the 280 km spacing.

The experiment with the soundings in the OZO determines a more relevant upper bound for the maximum forecast improvement achievable with a certain amount of targeted observations. Say, we could target 40 soundings anywhere on the northern hemisphere. If we had the hemispheric set of soundings at our disposal, we could, at least in principle, determine the subset of soundings of the hemispheric set that improves the forecast the most after the verification time through a series of assimilations and forecast for all different subsets. However, the number of subsets is astronomically large and the test requires computational resources

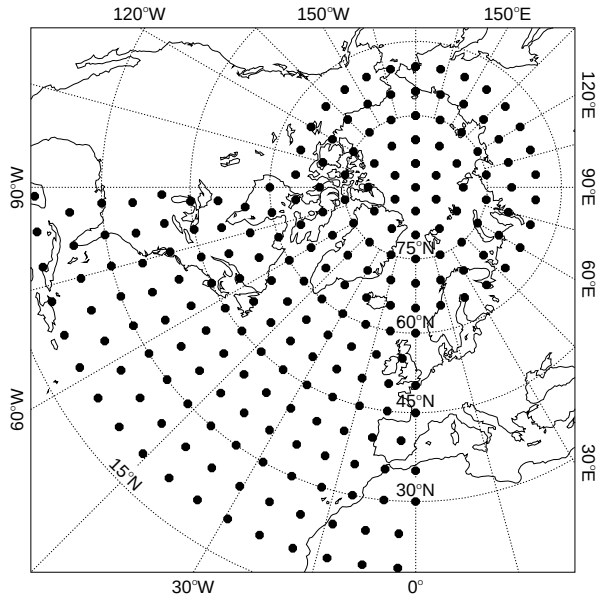

Fig. 1: Set of 219 locations from which 40 sounding locations are chosen randomly.

beyond imagination. Nevertheless, it is feasible to optimize the position of a rectangular domain. Here, a domain of the same size as the medium singular vector target regions is considered. It is sampled at the high spatial density with 40 soundings. The position of the domain is varied in discrete steps. The size of the steps is about half the width of the domain. Thus, one obtains a set of overlapping domains. The search for the OZO is limited to a wider neighbourhood of the singular vector targets. A number of about 15 rectangular domains will be tested for each case. The OZO is selected as the domain that minimizes the forecast error as measured with the total energy metric.

3 The First French Storm

In this section, we present results of the experiments for the violent storm that reached France in the early hours of 26 December 1999. The storm has been named (first) 'French' storm, 1999 Boxing Day low, Lothar and T1. Dynamical aspects of its life-cycle are discussed by Wernli *et al.* (2002). The system crossed the Atlantic at a high speed of about 30 $\mathrm{m\,s^{-1}}$. During this passage it is characterized as moderately intense shallow low-level cyclone. Rapid intensification occured when the cyclone passed to the cyclonic shear side of the jet axis during the 6 hours before it made landfall at the coast of Brittany. The central pressure dropped to its minimum value of 960 hPa close to Rouen around 6 UTC on 26 December. At 12 UTC the depression has reached Germany and its central pressure had risen again to 975 hPa. But the small-scale system was still accompanied by extreme pressure gradients. Along its track, maximum gust wind speeds in excess of 40 $\mathrm{m\,s^{-1}}$ were reported at many stations (e.g. 48 $\mathrm{m\,s^{-1}}$ in Paris and 55 $\mathrm{m\,s^{-1}}$ in the Swiss Middleland, see Pearce *et al.* 2001 and Wernli *et al.* 2002). Many people were killed in the storm. It caused huge damage to buildings and forests in France, Southern Germany, Switzerland and Austria. Several NWP models, which were operational at the time, had poorly forecasted this event in the short-range of 1–3 days. Assuming that these forecasting problems were entirely due to errors in the initial conditions, we determine the potential of improving a 2-day forecast of this event by using supplementary observations.

3.1 Control and Truth Forecasts

Forecasts were started from four different operational analyses dated 24 December 1999, 12 UTC to identify the control and truth forecasts. The analysis from Météo-France resulted in a forecast, that appeared best based on the subjective comparison of sea level pressure maps. Therefore, this forecast was chosen as truth. The forecast starting from the ECMWF analysis was selected as control; it is one of the poor forecasts. Figure 7a–c shows the sea level pressure maps of control and truth forecast and an ECMWF analysis valid at verification time, 26 December 12 UTC. The control forecast has two cyclones in the verification region. The eastern low with 983 hPa central pressure corresponds to the French storm. The low has a similar track as the observed storm but never attained the observed intensity. The western low, 976 hPa central pressure, is a system that is too intense in the control experiment. We will refer to this system as the *English storm*. There is an open wave in the analysis at its place. In the truth forecast, the English storm is absent and the French storm develops as deep cyclone with 968 hPa central pressure. According to the analysis and surface observations the French storm is 7 hPa too deep in the truth experiment at the verification time. However, six hours earlier the situation is reversed. A central pressure of about 960 hPa was observed, while the truth forecast has a central pressure of 968 hPa as 6 hours earlier. Overall, it seems justified to classify the truth experiment as a good forecast and the control experiment as a poor forecast. Now, as control and truth have been selected, no further reference to the actual system need be made. All required information is contained in the control and truth experiments as the latter is used for the verification and to construct the synthetic observations and the former provides the background field for the assimilation and the trajectory for the singular vector computations.

A crude upper bound of the best possible forecast improvement is obtained by using observations from the dense hemispheric network of 3393 radiosondes. With this hypothetical major upgrade of the observing network the truth forecast is almost replicated in terms of the sea-level pressure in the verification region (Fig. 7d). Disagreement between the hemispheric network experiment and truth becomes apparent with a root mean square measure of forecast error. As the analysis is a blend of the observational data with the wrong background fields, one would not expect to recover truth even with a very good observational coverage.

3.2 Singular Vectors and Target Regions

We will now see to what extent the singular vectors and the target regions diagnosed from them depend on the choice of the initial time norm. Figure 2 shows profiles and spectra of energy averaged over the leading five singular vectors. At initial time, the TESVs peak at 660 hPa whereas the HSVs peak around 450 hPa. Also, the partition between kinetic energy and potential energy depends on the initial time norm. For the HSVs, most energy is kinetic and for the TESVs, most energy is potential. Furthermore, the spectrum of the HSVs peaks around wavenumber 15 whereas the TESV spectrum is flatter with most of the energy at wavenumbers above 20. However, the evolved singular vectors are more similar. The evolved TESVs and HSVs are both dominated by the kinetic energy part; they peak both around 300 hPa and at wavenumber 10.

The structure of the TESVs at initial time is consistent with the familiar picture of baroclinic structures located in the lower and middle troposphere and tilted against the vertical shear. The HSVs have similar temperature perturbations with slightly larger spatial scales (Fig. 3). Upshear tilt is also apparent in the meridional velocity component for TESVs and HSVs. The structures of the zonal velocity component differ more between the two types of singular vectors. The TESVs exhibit highly tilted shallow structures which resemble the temperature perturbations, whereas the HSVs show deep structures with little tilt. We are currently investigating how the structure of the HSVs depends on the presence of observations in the Hessian metric. These results will be published elsewhere.

The geographical distribution of the initial time singular vectors is also dependent on the initial time norm.

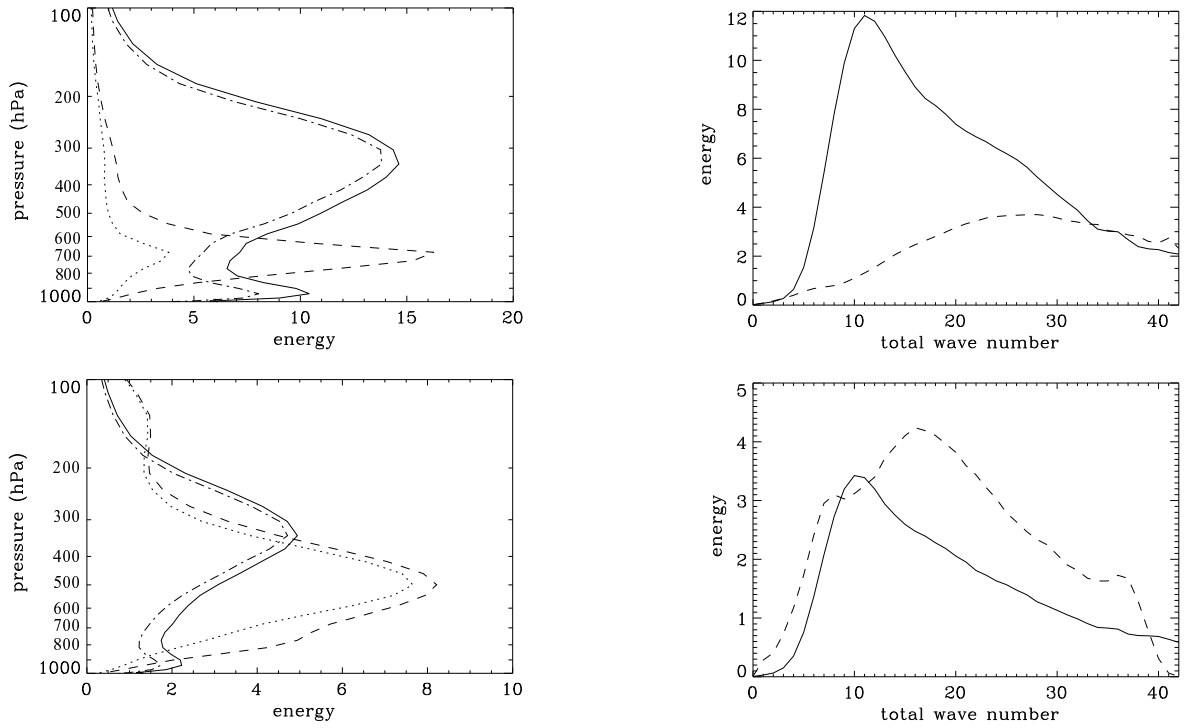

Fig. 2: Mean profile and mean spectra of total energy of the first five TESVs (top) and HSVs (bottom) for the French storm case. Initial time (dashed), final time (solid). Also shown are profiles of kinetic energy (dotted: initial time, chain-dashed: final time). Values at initial time are scaled by a factor of 100.

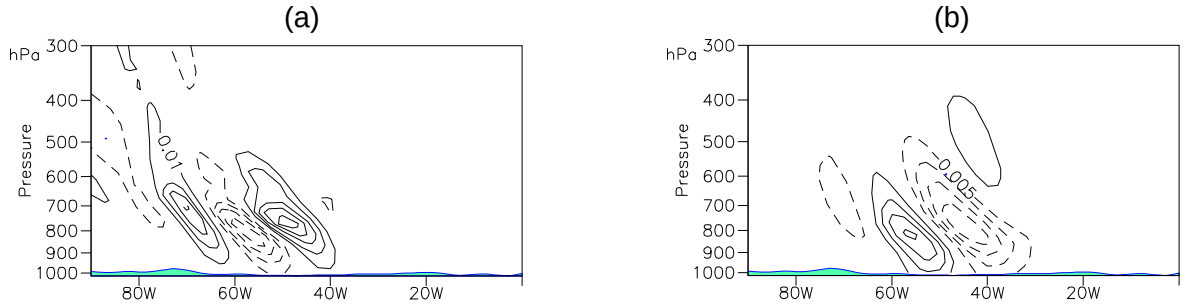

Fig. 3: Thermal structure at 45°N of the leading TESV (a) and the leading HSV (b) for the French storm case. The contour intervals are 0.01 K (TESV) and 0.005 K (HSV).

This results in differences of the target regions based on TESVs and HSVs (Fig. 4). The HSVs stay over the sea south of 50°N whereas the TESVs extend further over the continent up to 90°W. The position of the HSVs over the sea is favoured by the inhomogeneous distribution of observations. Initial errors are more constrained over the densely populated land areas than over the sea and other remote regions. The TESVs, on the contrary, are computed with a metric that is spatially uniform. To quantify the similarity of the target regions diagnosed from the two types of singular vectors, the number of sounding locations that targets of a given size have in common has been counted (Table 2). The large target regions ($12 \times 10^6\,\mathrm{km}^2$) based on the two types of singular vectors have about 70% of the soundings in common. The medium and small ($3, 0.9 \times 10^6\,\mathrm{km}^2$) target regions agree much less.

The target region depends on the location of the initial time singular vectors and the singular values which are used as weights in the function F. For both norms the singular value spectra are quite steep up to an SV index

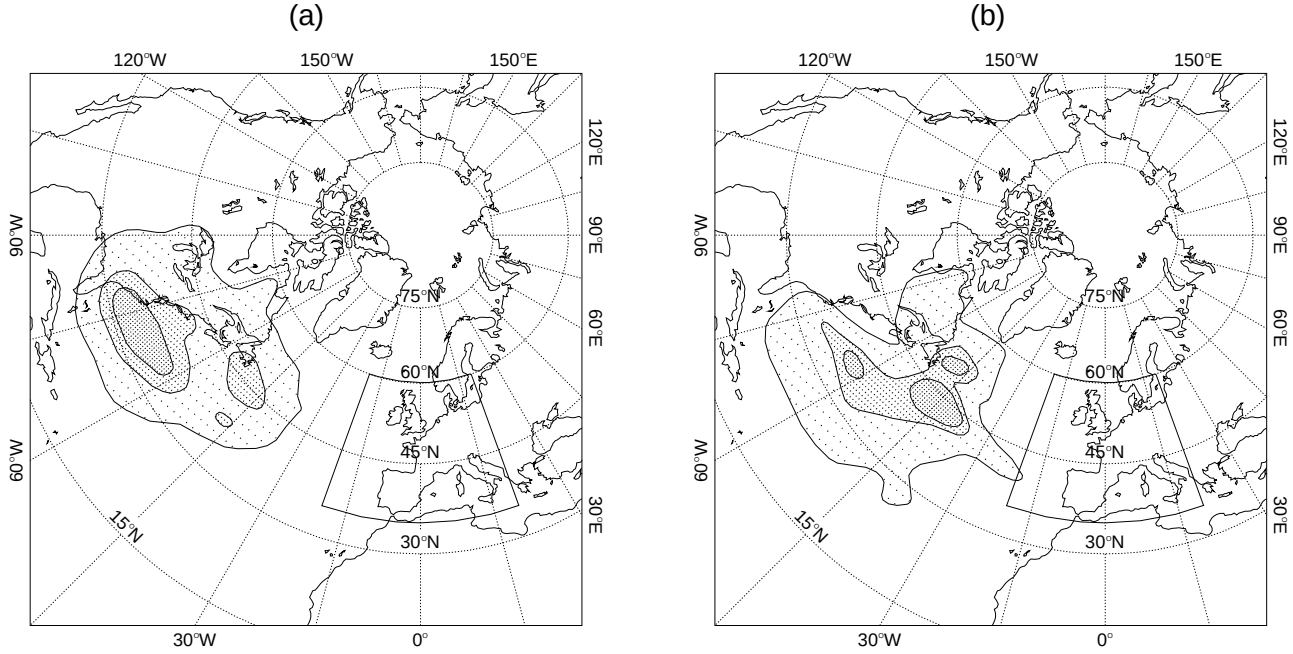

Fig. 4: Target regions (stippled) for French storm case based on TESVs (a) and based on HSVs (b). The sizes of the small, medium, and large region are 0.9, 3, and 12$\times 10^6$ km^2. The box indicates the verification region.

Tab. 2: Number of soundings locations that TESV-target and HSV-target have in common (1st entry) and total number of soundings in either type of target (2nd entry). French storm.

spacing	size of target region (10^6 km^2)		
Δs (km)	0.9 "small"	3.1 "medium"	12 "large"
280	1 / 10	14 / 40	110 / 160
560		4 / 10	29 / 40

of about 5 (Table 3). As a result, the target region changes relatively little if more singular vectors are included in the definition of F.

Maps of the synoptic situation at targeting time are plotted in Fig. 5. The fields are taken from the control experiment but the corresponding fields taken from the truth experiment look very similar. The low with a central pressure of 1007 hPa at 38°N, 60°W evolves into the cyclone that crosses France and Germany about 2 days later. The TESVs point primarily to the baroclinic zone in the lower troposphere upstream of this low. However, the HSVs highlight a region north east of the low where the jet maximum is located (45°N, 45°W).

Tab. 3: Singular values σ_i normalized with σ_1 for TESVs and HSVs; $\sigma_1 = 17.0$ (TESV) and 37.2 (HSV) for the French storm.

i	2	3	4	5	10	20
TESV	0.82	0.60	0.47	0.34	0.24	0.15
HSV	0.66	0.63	0.45	0.38	0.21	0.14

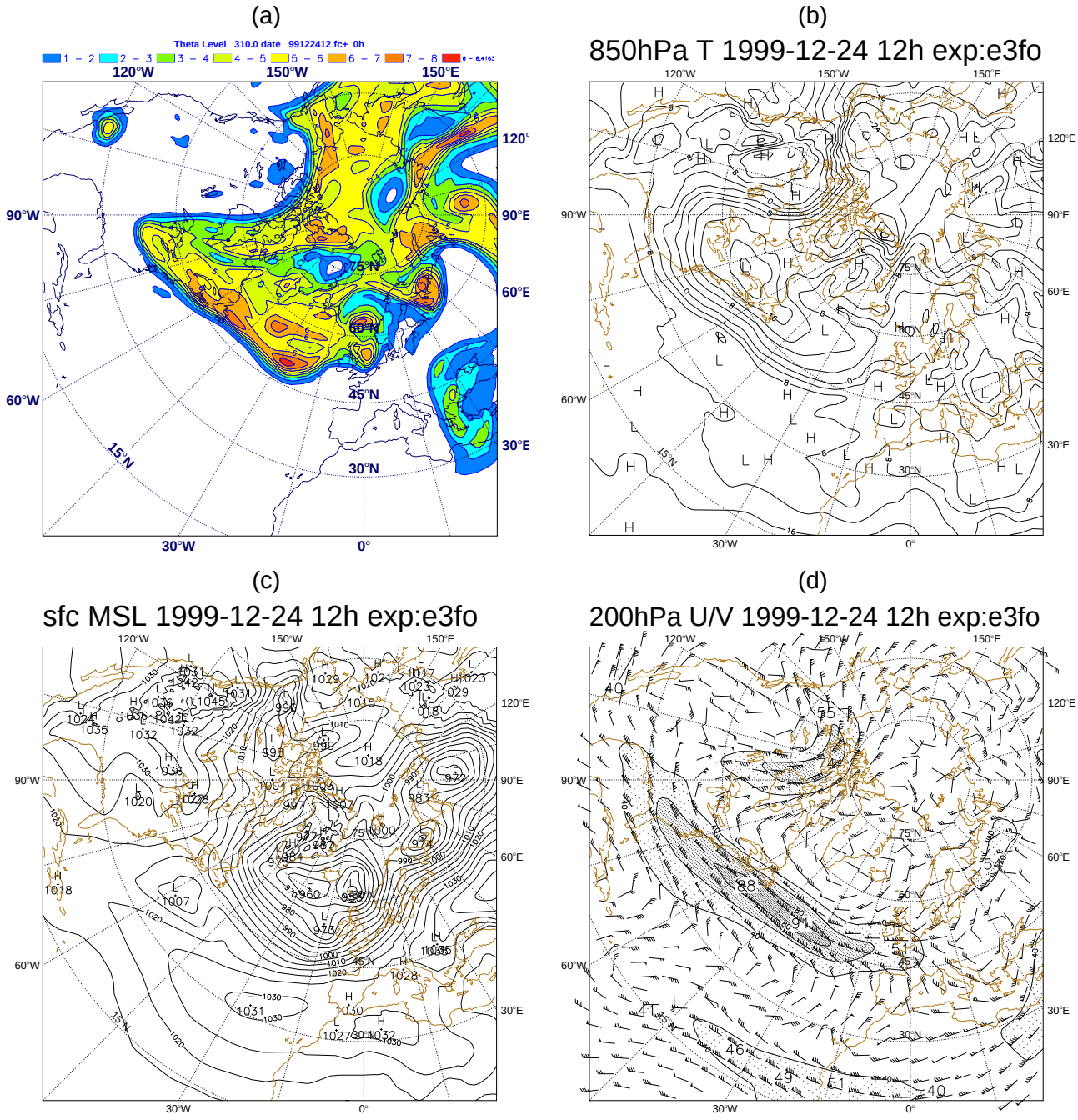

Fig. 5: Synoptic setting at observation time for the French storm case. (a) potential vorticity on the 310 K isentrope, (b) temperature at 850 hPa, (c) mean sea level pressure, and (d) wind at 200 hPa (shading: 40, 60, 80 m s^{-1}). Fields are taken from the control experiment.

3.3 Evaluation of Observation Targeting

Now, we discuss the results of impact experiments with 40 supplementary soundings. Singular vector targeting is compared with the OZO and the RDS. First, we check whether the singular vectors actually point to the OZO. Then, we inspect the forecast improvement apparent in sea-level pressure maps. This part of the evaluation is somewhat subjective but focuses on the synoptically relevant aspects of the forecast. Finally, the forecast

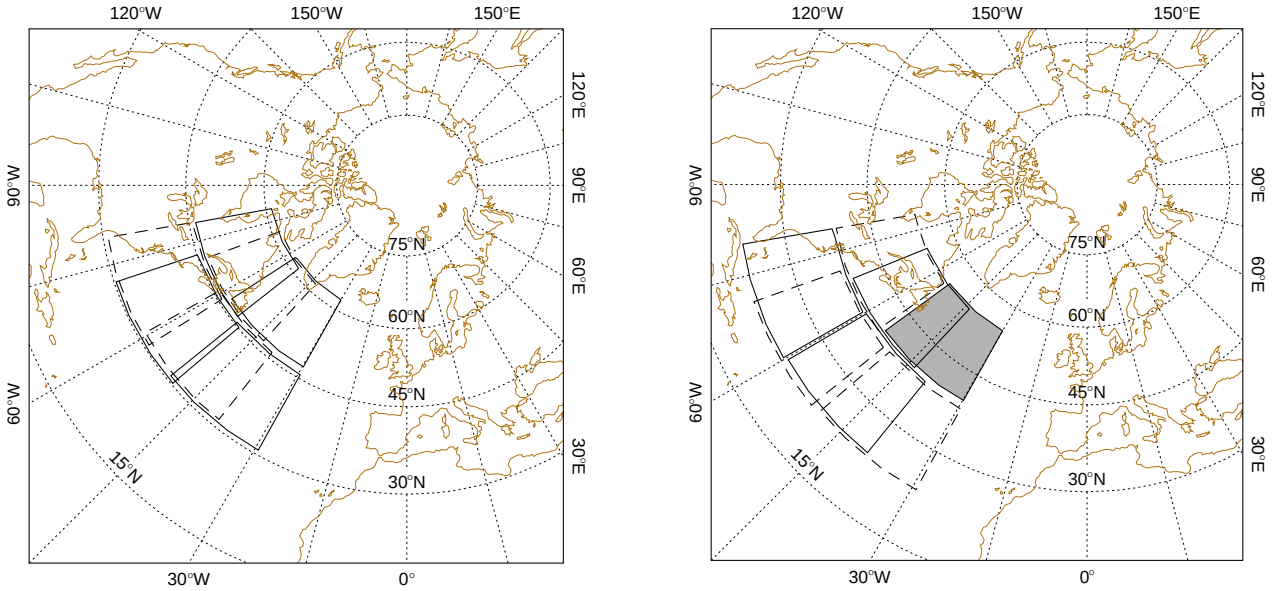

Fig. 6: The 14 rectangular domains in which the impact of supplementary observations was tested to determine the OZO (shaded domain) for the French storm case. The domain positions have been slightly shifted in the plot to enable the identification of the domain outlines.

improvements are compared quantitatively using the total energy metric.

The impact of 40 supplementary soundings was tested in 14 domains in order to determine the OZO (Fig. 6). The area of each domain is equal to the area of the medium-size singular vector targets. We based the choice of the OZO on a comparison of the forecast errors measured with the total energy metric in the verification region (see below). With this metric, the OZO turns out to be the zone 39°–54°N, 30°–54°W. The domains that are obtained by shifting the OZO approximately 7.5° to the South and to the North yield the second and third largest forecast error reduction, respectively. The errors of forecasts using soundings in these domains are 40% and 54% larger than the error obtained with the OZO. The sea-level pressure forecast in the experiment with supplementary observations in the OZO is close to the truth at the verification time (Fig. 7g). Intensity and position of the French storm are very accurate. However, there is still a weak wave present where the English storm is located in the control forecast.

Now, we turn to the question to what extent the medium-size singular vector targets agree with the OZO. Only a small part of the TESV-target points to the OZO; the TESV-target and the OZO have 7 of 40 sounding locations in common. The HSV-target agrees remarkably well with the OZO; they share 23 of the 40 sounding locations. The major part of the TESV-target and a smaller part of the HSV-target are located to the South-West of the OZO. As the HSVs point to the OZO and the TESVs highlight a different zone, we expect that the forecast using observations in the HSV-target has a smaller error than the forecast using observations in the TESV-target. The maps of the 48-hour sea-level pressure forecasts confirm this. The forecast that uses the observations in the medium-size TESV-target is already considerably better than the control forecast (Fig. 7e). The French storm becomes deeper and the English storm is replaced by a wave. However, an even more profound forecast improvement is obtained by using the observations in the medium-size HSV-target (Fig. 7f). In this experiment, the position and intensity errors of the French storm are even smaller and the English storm is removed completely. The forecast with the observations in the HSV-target is similar to the forecast with the OZO. The error reduction obtained with the five realizations of the RDS is variable (Fig. 7h-l). In terms of the sea-level pressure forecasts, the HSV-targeting beats all RDS experiments apart from realization E. TESV-targeting is better than realizations B and D.

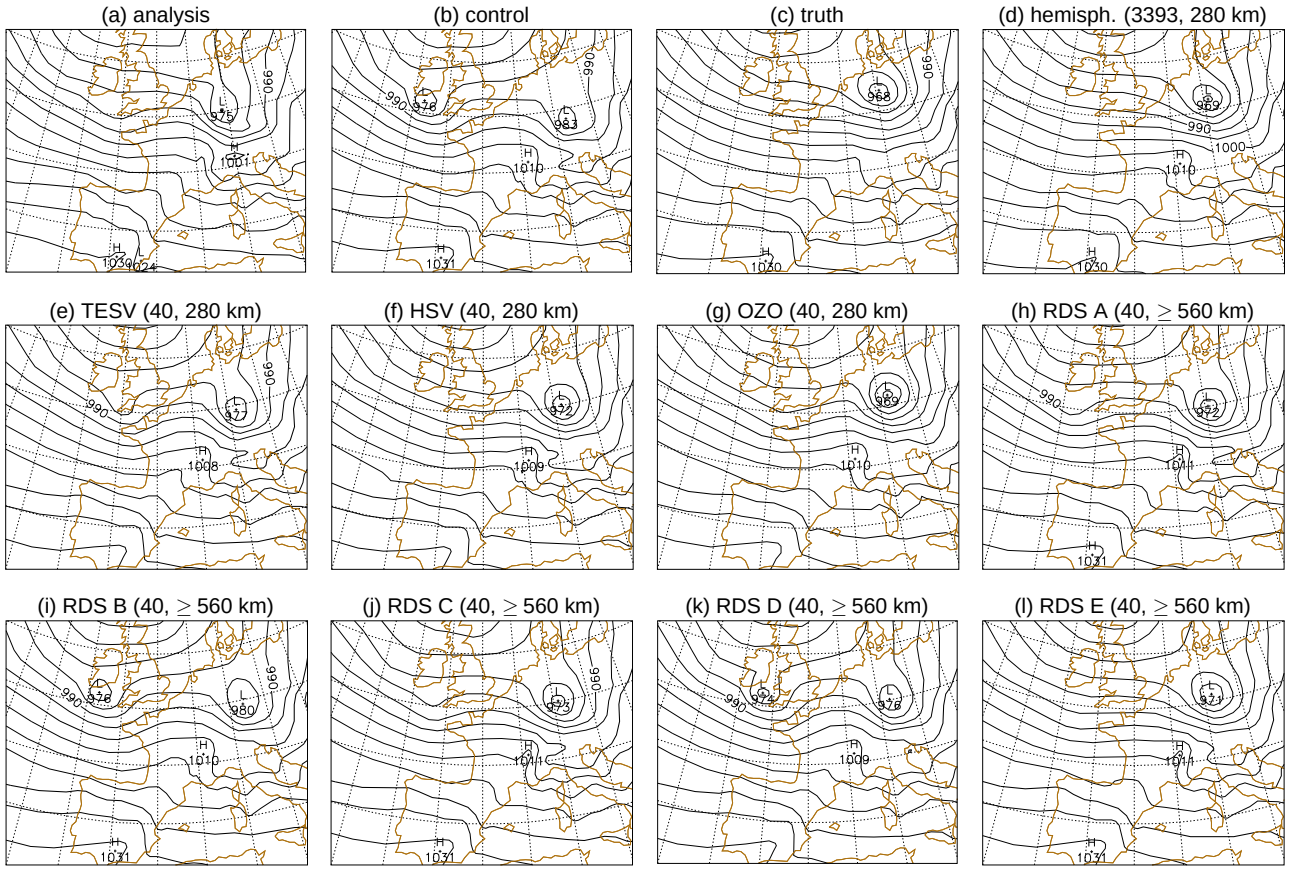

Fig. 7: Mean sea level pressure (every 5 hPa) at 26 Dec 1999, 12 UTC. (a) ECMWF-analysis, (b,c) 48-hour forecasts from the ECMWF analysis (control) and Météo-France analysis (truth), respectively, (d-l) 48-hour forecasts using supplementary observations. The number of soundings and their horizontal spacing are given in parentheses. See Table 1 and text for the different observing strategies.

For the quantitative comparison of the impact, we compute the total energy of the forecast error fields. These are given as the difference between the forecast and the truth experiment. The specific energy as defined by the first integrand in (1) is integrated in the verification region (20°W–20°E, 35°–60°N) from the surface to 500 hPa. Figure 8 shows the evolution of the error in the verification region. The error of the control experiment reaches a maximum at 54 h forecast lead time. This is during the mature phases of the English storm in the control experiment and the first French storm in the truth and control experiments. At 66 h forecast lead time, a low corresponding to the second French storm, also called T2 or Martin, enters the verification region in the truth experiment. In the control experiment, there is a slower moving low that does not enter the verification region until 72 h forecast lead time. The forecast error increases further when the second French storm enters the verification region in the truth experiment. In the interval from 36–60 h, the forecast error of almost all experiments using supplementary observations is significantly lower than the error of the control experiment. The signal from the additional observations in the OZO and the singular vector targets arrives at the verification region approximately at the beginning of this interval. As expected, the forecast using the hemispheric network of soundings provides a upper bound for the attainable forecast error reduction. With the hemispheric network, the error is reduced to 25% of the control error at 48 h, but only to 84% at 66 h, when the second French storm enters the verification region in the truth experiment. With the 40 soundings in the OZO, a large fraction of the error reduction obtained with the hemispheric network is achieved.

The superiority of the HSV-target over the TESV-target is also clear using the energy metric. The error of the

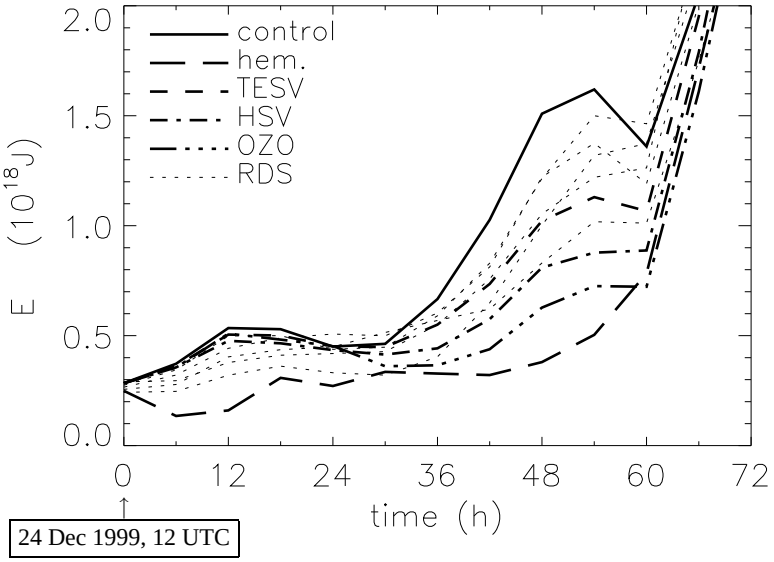

Fig. 8: Evolution of the forecast error for the French storm case. The total energy of the error fields is integrated from the surface to 500 hPa in the verification region (20°W–20°E, 35°–60°N).

experiment with the HSV-target is not much larger than that of the OZO experiment. Of the 14 domains tested to identify the OZO only the OZO itself leads to a smaller 48 h-forecast error than the HSV-target. Four of the 14 domains yield a smaller 48 h-forecast error than the TESV-target.

The forecast error differs considerably between the five realizations of the RDS. This is consistent with the picture conveyed by the sea-level pressure maps. Both singular vector techniques beat on average the RDS in the energy metric. Only one of the five realizations has a smaller forecast error than the experiment with the TESV-target. This realization (E) almost attains the error reduction obtained with the HSV-target. However, when the evaluation is based on the comparison of sea-level pressure maps, three of the five realizations are clearly better than the TESV-target.

One may expect that the number of soundings that happen to be in the vicinity of the OZO or the HSV-target controls the magnitude of the forecast error in the experiments with the RDS. However, these experiments do not show a clear anti-correlation between forecast error and the number of soundings in the sensitive region. This suggests that other factors such as the sampling pattern must be equally important for controling the error. Despite the lack of a clear anti-correlation, the good forecast of realization E suggests that a small number of, say 10, soundings soundings in the correct place could be sufficient to achieve a large reduction of forecast error. This conjecture is tested for regularly sampled singular vector targets with further experiments, which are discussed in section 5.

4 The Danish Storm

Now, we turn to the results of the experiments for the severe storm that crossed Denmark on 3 December 1999, known as ‘Danish’ storm or low ‘Anatol’. It was the most intense storm that hit Denmark in the 20th century according to a report of the Danish weather service; around 18 UTC on 3 December, the wind speed reached values of more than 34 $\mathrm{m\,s^{-1}}$ at Danish and German coastal stations; maximum gust wind speeds of more than 50 $\mathrm{m\,s^{-1}}$ were reported (`http://www.dmi.dk/vejr/aktuelt/199912090000/orkan.pdf`). The surface low formed around 18 UTC on 2 December west of Ireland and rapidly deepended from 0–12 UTC on

the next day. The low attained its minimum central pressure of 953 hPa at 18 UTC on 3 December, when it was located just off the east coast of Jytland (Ulbrich *et al.* 2001). Some operational numerical models provided poor forecasts of this event in the range 1–3 days. Following the same procedure as for the French storm case, we evaluate singular vector based observation targeting in a perfect model scenario.

4.1 Control and Truth Forecasts

Forecasts were run from the four different operational analyses valid on 1 December 1999, 12 UTC. The Danish storm was reasonably well forecast at 2-day range in the simulation starting from the Météo-France analysis and in that using the ECMWF analysis. The latter analysis was selected to represent the truth. At verification time, the Danish storm is forecast as a low with 969 hPa central pressure in the truth experiment whereas a central pressure of about 960 hPa was observed (Fig. 12a,c). The forecast initialized with the DWD analysis is poor; it is chosen as the control. It has a shallow low of 986 hPa central pressure instead of the storm (Fig. 12b).

The potential of improving the forecast with supplementary observations is smaller in this case than for the first French storm. A low with 975 hPa central pressure is forecast in the experiment with the hemispheric network of soundings. Thus, even if the entire region upstream of the verification region is observed well, an error in central pressure of 6 hPa remains. As already mentioned, the reason for this deviation from truth is that the assimilation blends information from the perfect observations with information from the erroneous background fields.

4.2 Singular Vectors and Target Regions

The general structure of TESVs and HSVs is fairly similar to that of the corresponding singular vectors in the French storm case. The HSVs also exhibit baroclinic temperature perturbations which are tilted against the vertical shear. The amplitude of the temperature perturbations of the HSVs is considerably smaller than that of the TESVs; this is consistent with the different split between kinetic energy and potential energy for the two types of singular vectors. Again, the spectrum of the TESVs is flatter than the spectrum of the HSVs. In this case however, the peak of energy is located at about the same level, around 550 hPa, for both types of singular vectors.

The target regions diagnosed from the leading TESVs and the leading HSVs are plotted in Fig. 9. The large targets have a large meridional extension from 25°N to 75°N. But the core of the targets with the highest values of the function F is north of 45°N. It extends from the Hudson Bay into the North-Western Atlantic. The choice of the initial time singular vector norm affects the target region to some extent. But the disparity between the target regions is less pronounced than it was for the French storm. The number of sounding locations that a TESV-target and a HSV-target of the same size share is given in Table 4. The larger the size of the target region is, the greater is the level of agreement between two corresponding targets. In this section we will discuss the impact of 40 soundings in the medium targets at a horizontal spacing of 280 km. For this sampling strategy, 24 of the 40 sounding locations agree.

The synoptic environment of the targets is illustrated in Fig. 10 with fields taken from the control experiment. The low that evolves into the Danish storm forms around 0 UTC on 3 December. The system can be traced further backwards in time in the 850 hPa vorticity field. The positive vorticity anomaly associated with the system is spawned around the targeting time from the parent low (991 hPa central pressure) located at 41°N, 65°W. The southerly part of the large target regions lies to the East and the South of the parent low. But the medium-size targets are located well to the North of the parent low. Zones with large lower-tropospheric baroclinicity can be identified at the north-western and south-eastern ends of the medium-size target regions. In

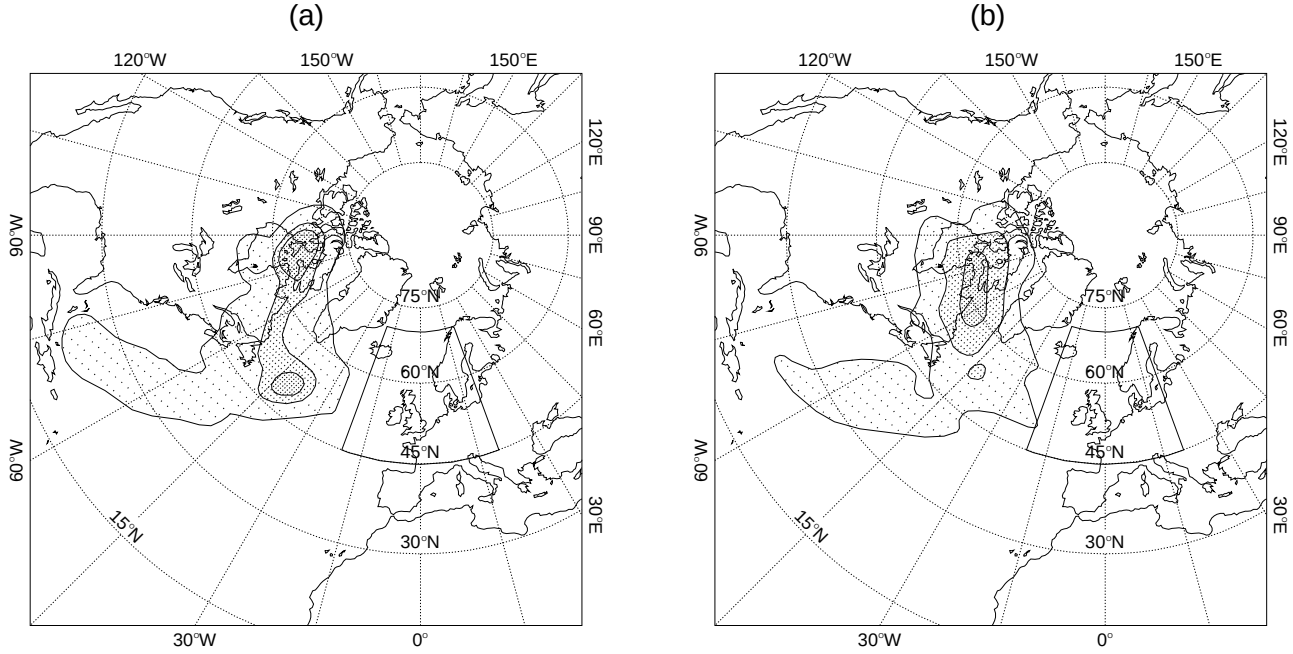

Fig. 9: Target regions (stippled) for the Danish storm case based on TESVs (a) and based on HSVs (b). The sizes of the small, medium, and large region are 0.9, 3, and 12$\times 10^6$ km^2. The box indicates the verification region.

Tab. 4: Number of soundings locations that TESV-target and HSV-target have in common (1st entry); total number of soundings in either type of target (2nd entry). Danish storm.

spacing	size of target region (10^6 km^2)		
Δs (km)	0.9 "small"	3.1 "medium"	12 "large"
280	3 / 10	24 / 40	136 / 160
560		6 / 10	35 / 40

the area between, the baroclinicity is quite low, however. In the potential vorticity field at the 310 K isentropic level, two prominent structures are apparent. The patch of potential vorticity that is nearly cut off from the main vortex around 75°W and 35°N and the potential vorticity filament around 105°W. The singular vectors focus on a region of large potential vorticity gradients at the edge of the polar vortex in the vicinity of the cutting-off process. The vortex edge exhibits a distinct kink to the north of the cut-off and a local maximum of potential vorticity. The potential vorticity anomaly associated with this kink will later interact with the tropospheric vorticity maximum spawned from the parent low to form the Danish storm. Thus, with hindsight it is perhaps plausible why the region highlighted by the singular vectors is dynamically sensitive.

4.3 Evaluation of Observation Targeting

The impact of supplementary soundings was tested for the 15 domains shown in Fig. 11 to identify the OZO. The smallest forecast error measured with the total energy metric is obtained with the domain 48°–61°N, 40°–69°W. The domains yielding the second and third largest forecast error reduction are located to the East and South-East of the OZO. The forecast error in these experiments is about 35% larger than the forecast error obtained with the OZO. The intensity and position error of the storm in the OZO experiment are similar to the errors in the experiment with the hemispheric network (Fig. 12d,g). As we will see later, the additional

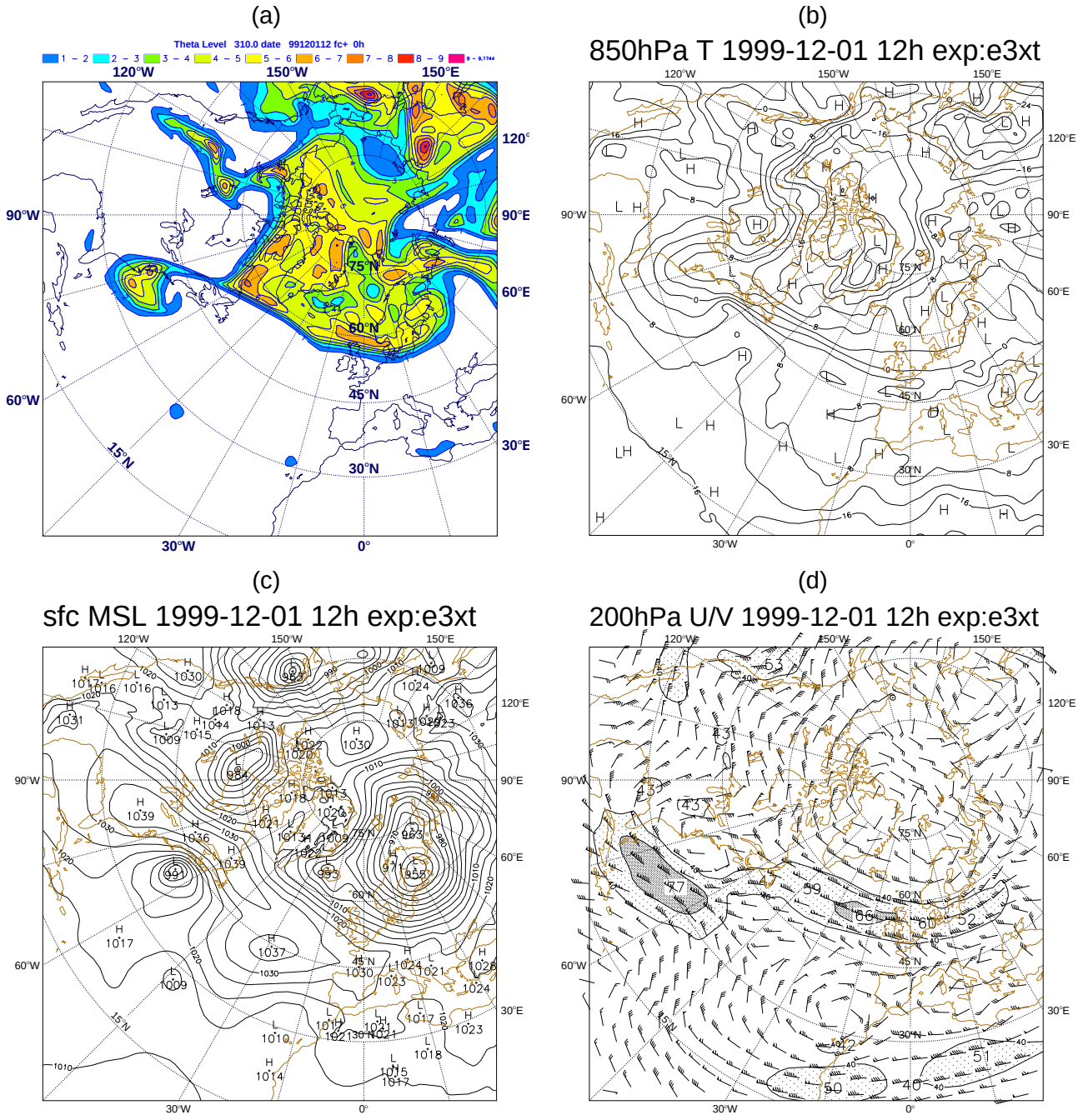

Fig. 10: Synoptic setting at observation time for the Danish storm case. (a) potential vorticity on the 310 K isentrope, (b) temperature at 850 hPa, (c) mean sea level pressure, and (d) wind at 200 hPa (shading: 40, 60, 80 m s^{-1}). Fields are taken from the control experiment.

observations of the hemispheric network still considerably improve the forecast in terms of the total energy of the error integrated over the verification region. This further improvement is associated with a better forecast of the large-scale pattern in the verification region. For instance, the position of the trough situated between Iceland and the British Isles is closer to the truth in the experiment with the hemispheric network than in the experiments with the OZO.

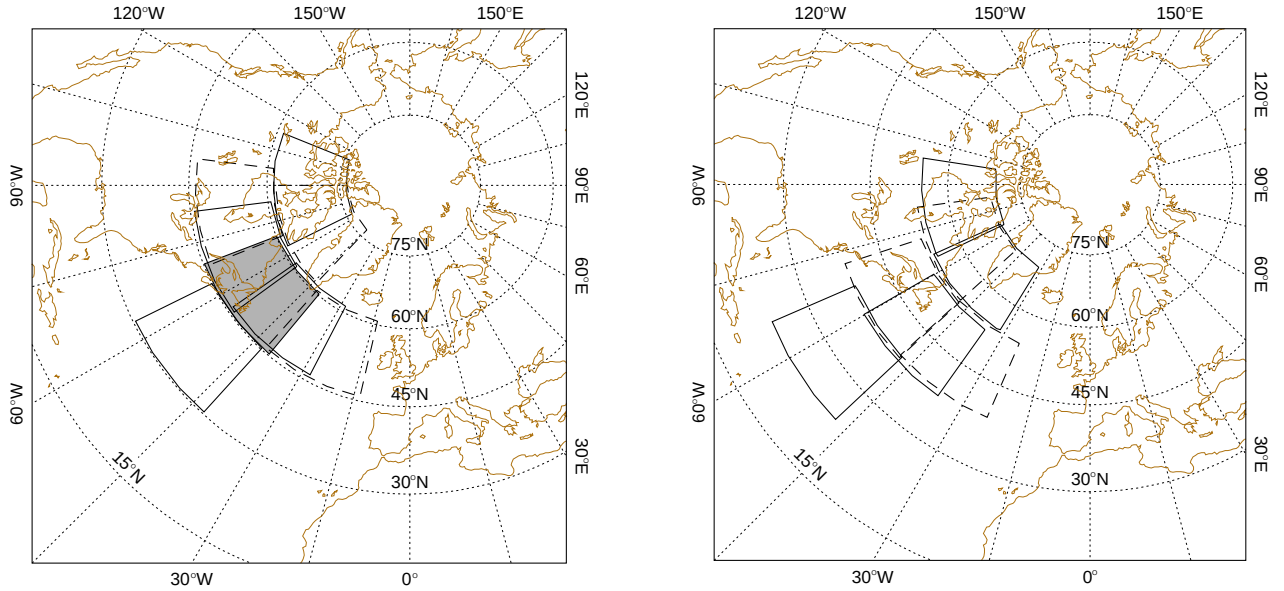

Fig. 11: The 15 rectangular domains in which the impact of supplementary observations was tested to determine the OZO (shaded domain) for the Danish storm case. The domain positions have been slightly shifted in the plot to enable the identification of the domain outlines.

Both types of singular vectors point to the OZO. The medium size targets diagnosed from TESVs and from HSVs share each 16 of 40 sounding locations with the OZO. The singular vector targets are biased towards the North-West compared to the OZO. As the HSV-target and the TESV-target are quite similar we expect only minor differences between the forecasts using the two different targets. This expectation is confirmed by the sea-level pressure forecasts (Fig. 12e,f). Both singular vector experiments forecast the low with a central pressure of about 978 hPa at a location 250 km to the South-West of the position of the low in the truth experiment. The low in the HSV experiment is slightly deeper. According to the sea level pressure maps, a major fraction of the forecast improvement obtained with the OZO is achieved with singular vector targeting. All five experiments using the RDS result in forecasts which are worse than the forecasts using soundings in the singular vector targets. Only realization D almost reaches the forecast improvement obtained with the singular vector targets.

Next, we compare the forecasts quantitatively using the total energy of the forecast error integrated in the verification region (45°–70°N, 20°W–20°E) from the surface to 500 hPa as measure of skill. Figure 13 shows the evolution of the errors. The error in the control experiment reaches its maximum 6 h after the verification time. After this maximum, the error decreases as the storm weakens in the truth experiment and moves out of the verification region. Up to 60 hours into the forecast, the experiment with the OZO has the smallest error of all experiments using 40 supplementary soundings. At the verification time, the forecast error reduction using the OZO is about half of the reduction obtained with the hemispheric network. The singular vector targets yield about a fourth of the error reduction obtained with the hemispheric network. The HSV-target is worse than the TESV-target from the verification time onwards. At a forecast range of 66 h, the error in the HSV-experiment becomes even larger than the control error. When the forecast skill is measured with total energy of forecast error integrated over the verification region, the improvement associated with the singular vector based targeting appears quite moderate as compared with the typical improvement obtained with the RDS. Only realization C has a larger forecast error than the singular vector experiments.

The order of the experiments in terms of their skill measured with total energy of forecast error in the verification region is not consistent with the ranking that is suggested by the sea-level pressure maps. This inconsistency

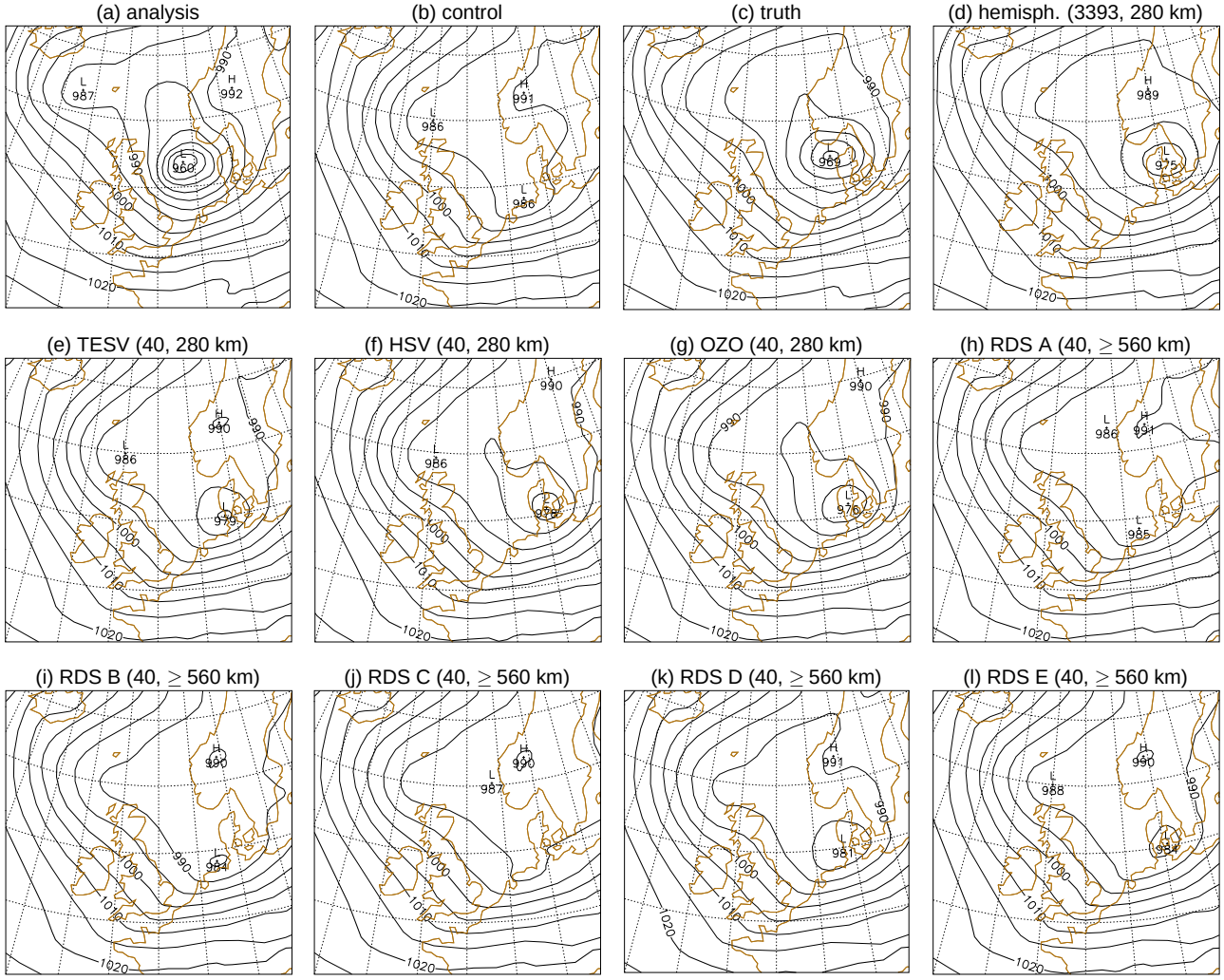

Fig. 12: Mean sea level pressure (every 5 hPa) at 3 Dec 1999, 12 UTC. (a) ECMWF-analysis, (b,c) 48-hour forecasts from the DWD analysis (control) and ECMWF analysis (truth), respectively, (d-l) 48-hour forecasts using supplementary observations. The number of soundings and their horizontal spacing are given in parentheses. See Table 1 and text for the different observing strategies.

may be due to errors in the upper air fields that do not manifest themselves in the sea-level pressure field or it may be due to errors of the forecast of the larger scale flow in the verification region. To identify the cause of the inconsistency, we computed the total energy of the 48 h forecast error also in a smaller box centred at the position of the storm (50°–60°N, 0°–20°E); we will refer to this region as the storm environment. Its area is a fourth of the area of the verification region. For the control experiment, the error in the storm environment region contributes to half of the error in the verification region. Thus, errors not associated with the storm itself may conceal the forecast improvement achieved for the Danish storm with the targeted observations. Table 5 contains the forecast error for both regions for the impact experiments. The errors computed in the storm environment region are more consistent with the impression obtained from the sea-level pressure maps. The singular vector targets beat the RDS in this metric clearly. Only realization E results in a slightly smaller error than the singular vector targets. The HSVs are somewhat superior to the TESVs. Furthermore, the experiment with the OZO nearly reaches the error reduction obtained with the hemispheric network. Overall, the localized distributions of observations in the OZO and the singular vector targets reduce the error more efficiently in the storm environment than in the entire verification region. With the RDS, on the contrary, a larger area is sampled

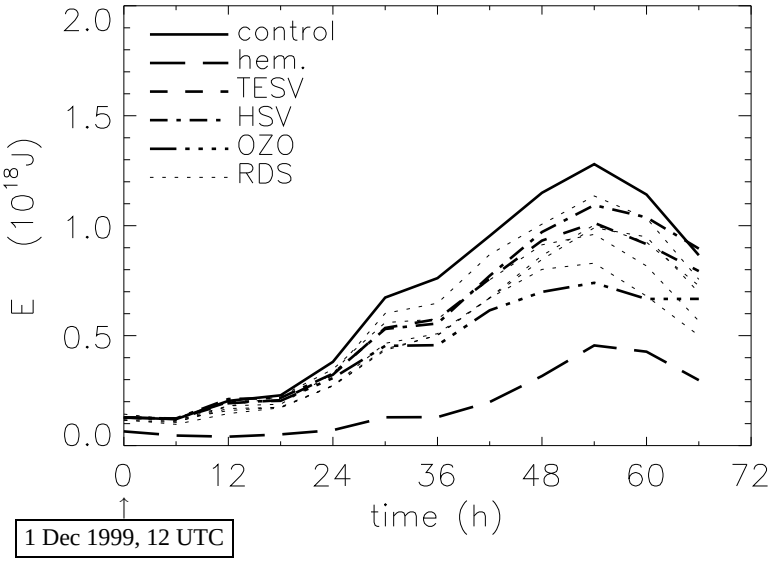

Fig. 13: Evolution of the forecast error for the Danish storm case. The total energy of the error fields is integrated from the surface to 500 hPa in the verification region (20°W–20°E, 45°–70°N).

with the soundings, therefore it is not surprising to find that the RDS performs better at reducing the large-scale error.

Tab. 5: Total energy of 48-hour forecast errors integrated over the verification region (VR, 45°–70°N, 20°W–20°E) and the storm environment (SE, 50°–60°N, 0°–20°E) for the Danish storm. The errors (in percent) are normalized with the corresponding error of the control experiment.

Exp.	OZO	TESV	HSV	RDS A	RDS B	RDS C	RDS D	RDS E
VR	61	81	84	70	74	88	79	75
SE	43	71	67	83	80	105	74	65

5 Sensitivity to Target Region Size and Sampling

In the previous sections, the impact of 40 supplementary soundings sampling target regions with an area of 3×10^6 km^2 was evaluated. One can argue that in practice there will be economic and other constraints which limit the number of additional observations and perhaps also the region that could be sampled with the observations. Given these constraints, the task of targeting is to find the optimal distribution of the observations. However, one could view the targeting problem more generally. Say, we wanted to invest observational resources to achieve a certain reduction of the forecast uncertainty; but there was some flexibility concerning the amount and or type of the observational resources that could be added. Then the task of targeting should include the specification of adequate constraints to achieve this forecasting goal. In terms of the simple constraints used in this work, the questions are: What is an adequate size of the target region to achieve a significant forecast improvement? How many soundings are required to sample this target region well enough to achieve the forecast improvement? Here, we discuss additional impact experiments designed to answer these questions after the fact for the two storms.

Four additional experiments were performed for each singular vector type (see Table 1 for an overview of

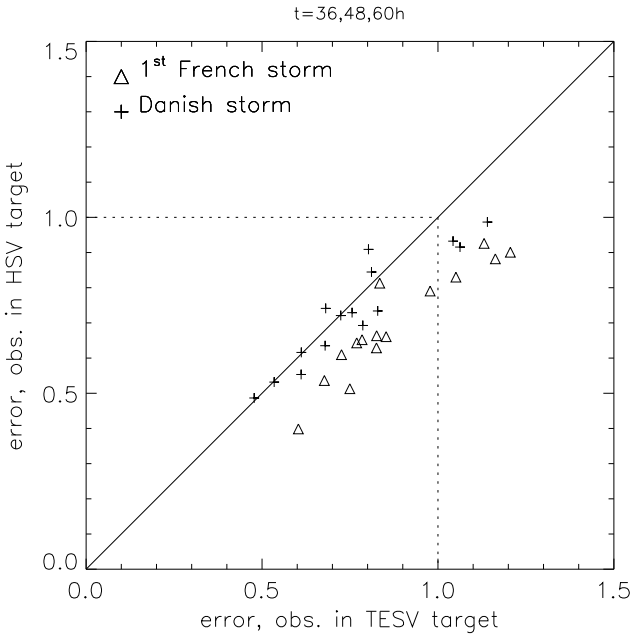

Fig. 14: Forecast error of experiments using TESV targets versus forecast errors of experiments using HSV targets. The error is computed with the total energy metric as in Fig. 8 and normalized with the error of the control experiment. The 15 symbols for each case correspond to the five pairs of experiments (cf. Table 1) and the 3 forecast ranges 36, 48, 60 hours.

the different experiments). The impact of additional observations is determined for the small target region (0.9×10^6 km^2) and the large target region (12×10^6 km^2) with 280 km spacing between soundings. This requires 10 and 160 soundings, respectively. The two other experiments test the low spatial density of the soundings for the medium and large target regions. With the 560 km spacing, 10 and 40 soundings are required. As in the previous sections, we will examine the impact apparent in sea-level pressure maps and quantitatively compare forecast errors using the total energy metric.

First, we summarize the differences in impact that are apparent in sea-level pressure maps (maps not shown). For each choice of target region size and sampling density, the experiment using observations in the HSV target is superior to the corresponding experiment using observations in the TESV target. The better performance of the HSV targets is very pronounced for the medium and small target regions. Ten soundings in the medium sized target region computed with HSVs appear to be very efficient in improving the forecast. On the contrary, the forecasts with 10 soundings in the small and medium TESV-targets are quite poor. Observations in the large TESV targets lead to quite a large forecast improvement. This is not suprising as the large target region computed with TESVs has a considerable overlap with the OZO. For the Danish storm, the forecasts using observations in TESV-targets are quite similar to the corresponding forecasts using the same target region size and observation density but HSVs.

The impression about the relative performance of TESV-targeting and HSV-targeting deduced from the sea-level pressure maps is consistent with forecast errors quantified in terms of total energy in the verification region (Fig. 14). The Hessian metric is clearly superior for targeting to the total energy metric in the French storm case. In the Danish storm case, the two types of singular vectors perform about equally well. However, HSV-targeting is always better than TESV-targeting for both cases, if 48 h forecast errors are compared for the storm environment regions. But the advantage of using the Hessian metric is more pronounced in the French storm case.

Now, we turn to the primary question of the adequate size of the target region and the adequate spatial density

Tab. 6: Scaled errors of the 48-hour forecasts using soundings in HSV-target regions. Errors quantified with total energy in verification region, total energy in storm environment region, central pressure, and position of the low centre.

spacing	number of	$(\varepsilon - \varepsilon_{hem}) \,/\, (\varepsilon_{cntl} - \varepsilon_{hem})$			
Δs (km)	soundings	TE_{VR}	TE_{SE}	pressure	position
280	10	0.77	0.84	0.44	0.73
560	10	0.72	0.81	0.30	0.70
280	40	0.38	0.46	0.20	0.45
560	40	0.35	0.37	0.13	0.23
280	160	0.20	0.25	0.14	0.17

Tab. 7: as Table 6 but for the Danish storm.

spacing	number of	$(\varepsilon - \varepsilon_{hem}) \,/\, (\varepsilon_{cntl} - \varepsilon_{hem})$			
Δs (km)	soundings	TE_{VR}	TE_{SE}	pressure	position
280	10	0.91	0.95	1.04	0.83
560	10	0.63	0.29	0.47	0.20
280	40	0.79	0.46	0.29	0.20
560	40	0.47	0.06	0.48	0.21
280	160	0.38	0.01	0.06	−0.16

of observations sampling the target. We focus on targeting with HSVs as these were found to yield superior targets than TESVs for all target region sizes. Based on the forecast improvement apparent in the sea-level pressure maps, we conclude that an area of 3×10^6 km^2, which corresponds to the medium target region size, is adequate to achieve a significant forecast improvement. The forecast improvement obtained with the small target regions is already noticable for the first French storm but it is negligible for the Danish storm. A large fraction of the possible forecast improvement is obtained if the medium size target region is sampled with just 10 soundings.

However, the adequate size and sampling density depend on the measure of forecast accuracy that is being used. To illustrate, we look at the following objective measures: the total energy of forecast error in the verification region and in the storm environment region, and also the errors in central pressure and position of the low. These errors are given in tables 6 and 7 using the scaling $(\varepsilon - \varepsilon_{hem})/(\varepsilon_{cntl} - \varepsilon_{hem})$. A scaled error of 0 corresponds to the error ε_{hem} obtained with the hemispheric network and a scaled error of 1 corresponds to the error ε_{cntl} of the control experiment. Half of the forecast improvement that could be obtained with the hemispheric network may be considered as a reasonable goal that should be achieved with the targeted observations. This goal corresponds to a scaled error of less than 0.5. All experiments with the medium and large target regions meet this goal if forecast skill is measured with the central pressure error. However, if skill is measured with the total energy of the forecast error in the verification region the goal is more difficult to achieve. The low spatial density in the medium size target region is not sufficient for the French storm; at least 40 soundings are required in the medium or large target region. For the Danish storm, at least 40 soundings are required in the large target region to meet the goal. If the total energy of the forecast error is integrated only over the storm environment, 10 or more soundings in the medium target region are sufficient to achieve the goal in the latter case. The same holds for the position error of the Danish storm. For the French storm, on the other hand, it is not possible to achieve the goal for the position error and the forecast error in the storm environment (45°–55°N, 0°–20°W) with 10 soundings.

The results of the sensitivity experiments in this section could be interpreted differently. In a scenario, in which the number of soundings is fixed, the optimal spacing between them needs to be determined. Therefore, it is of

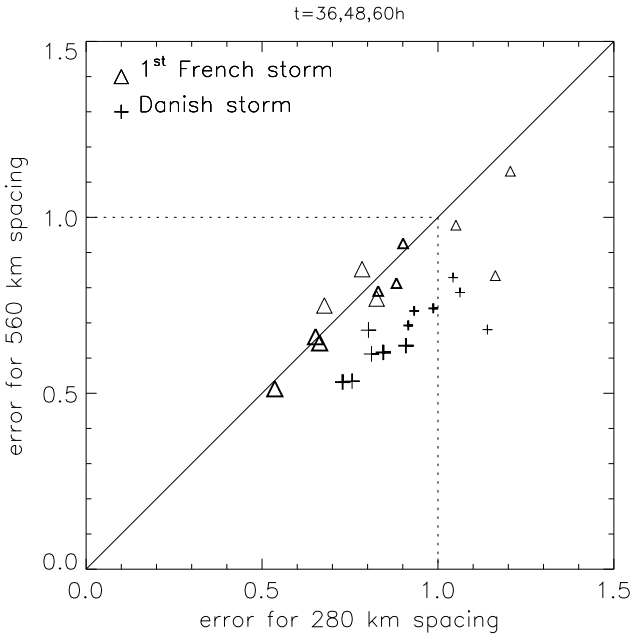

Fig. 15: Forecast error of experiments in which a singular vector target is sampled with N soundings at 560 km spacing versus the error of the corresponding experiments in which the central region of the target is sampled with N soundings at 280 km spacing. Errors are computed as in Fig. 14. The 12 symbols correspond to the TESV targets and the HSV targets (bold symbols), $N = 10$ *and 40 (large symbols) soundings, and the 3 forecast ranges.*

interest whether the 560 km spacing or the 280 km spacing yields the larger forecast error reduction. Forecast errors measured with the total energy metric are compared in Fig. 15. Each symbol corresponds to a pair of experiments using the same number of soundings and the same singular vector type. For the Danish storm, the 560 km spacing is clearly superior to the 280 km spacing. The superiority of the coarser spacing is also evident from the sea-level pressure maps for the experiments with 10 soundings. However, in the experiments with 40 soundings the coarser spacing does not yield a better sea level pressure forecast. For the French storm, the coarser spacing is superior for 10 and for 40 soundings for the sea-level pressure forecast, but there is little difference between the two spacings in terms of the total energy metric (Fig. 15). Overall, the 560 km spacing appears somewhat better than the 280 km spacing for the two cases.

For a fixed target region size, one would expect that the forecast error decreases when the density of the additional observations is increased. This is true for the French storm. The higher spatial density results in smaller forecast errors measured with the total energy metric. The positive impact of the higher spatial resolution is also evident in the sea level pressure maps for the experiments with the medium target but not for the experiments with the large target. In the Danish storm case, the impact of increasing the spatial resolution of the observations is overall neutral. For the medium size target region, the higher spatial density even yields a larger forecast error measured with the total energy metric, but the sea-level pressure forecast appears similar to the one with the low spatial density.

6 Observational Error

All experiments discussed so far used observations that have no observational error apart from small interpolation errors. The aim of this section is to determine the effect of observational errors on the forecast error. For the

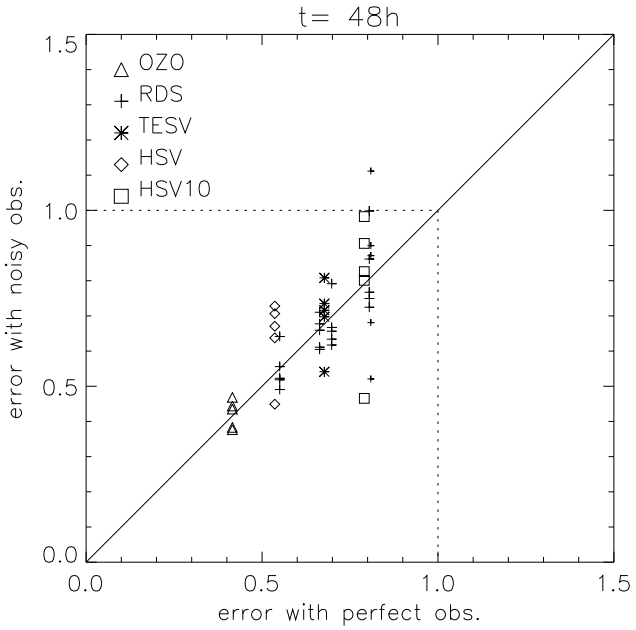

Fig. 16: Impact of observational error on the forecast error. Forecast errors are computed as in Fig. 14. All experiments, except HSV10, use 40 soundings. French storm case, 48 h forecast lead time.

case of the French storm, we repeat the analysis/forecast experiments for some configurations of observing sites adding perturbations to the observed values taken from the truth run. The perturbations are constructed with a random number generator in order to represent normally distributed errors, which are uncorrelated between different observations and which have the same variance as the observation error estimate used for radiosonde data in the assimilation scheme. In order to get a crude estimate of the distribution of forecast errors due to this distribution of observation errors we repeated each experiment five times with different realizations of the random numbers. Experiments with perturbed observations were run for the following configurations of 40 sounding locations: the OZO, the five realizations of the RDS and the two medium-size singular vector targets. In addition, the experiment with 10 soundings in the medium-size HSV-target was rerun with perturbed observations.

The forecast errors of the experiments with perturbed observations are plotted versus the forecast error of the corresponding experiment with perfect observations in Fig. 16 using the total energy metric localized to the verification region. The errors of forecasts using perturbed observations scatter around the error of the forecast using perfect observations. The use of perturbed observations yields a more accurate forecast than the use of perfect observations for 44% of the realizations if the average over the nine different configurations of sounding locations is taken. This may appear surprising at first. However, in the appendix it is shown that for sufficiently “small” observational errors half of the realizations of observational error are expected to improve the forecast compared to the forecast using perfect observations. Observational errors are small in this context if their contribution to the forecast error is small in magnitude compared to the contribution arising from the background error. The latter corresponds to the first term in (A4) in the appendix and the contribution from observational error to the last term in that equation. The scatter of forecast error in the regime of small observational errors is due to the second term describing the superposition of the error from the background and the error from observations. This term is linear in the observational error and therefore vanishes in the mean over all realizations. A closer inspection of Fig. 16 shows that forecast improvement compared to the forecast using perfect observations occurs considerably more often in the subset of RDS experiments than in the rest of experiments, in which the soundings are located in a sensitive region. In the latter experiments, we expect that

the contribution of the error from the background field (observations) to the forecast error is smaller (larger) compared to the RDS experiments. Thus, the quadratic contribution of the observational error to the forecast error in (A4) becomes more important and a worse forecast compared to the forecast using perfect observations more likely.

The forecast error exhibits a larger spread in the perturbed observation experiments with 10 soundings in the HSV-target than in the experiments with 40 soundings in the HSV-target. This difference is also noticable in the errors of position and the central pressure of the low for the two different sampling densities. The central pressure of the French storm ranges from 971 to 974 hPa in the set of experiments with 40 soundings and it ranges from 967 to 979 hPa in the set of experiments with 10 soundings. The reason for this behaviour is that more observations affect an analysis grid point at the higher observation density and thus the magnitude of the analysis perturbation due to observational errors is likely to be smaller. A simple analogy is the zero-dimensional case, in which a single quantity is measured several times. The expected standard deviation of the average of n measurements decreases as $n^{-1/2}$ assuming uncorrelated errors.

7 Discussion and Conclusions

In this study we evaluated the potential to improve poor forecasts of two severe extra-tropical storms by using supplementary observations in regions identified with singular vectors. There are several key differences between this evaluation and the numerous impact studies using data from previous field experiments. The singular vector targets were compared with the optimal zone for observing (OZO) and the impact of targeted observations was compared with that of un-targeted distributions of observations (RDS). Furthermore, the test of Hessian singular vectors for targeting is novel. The sampling strategy also deviates from current targeting practice. The target regions were sampled with a two-dimensional pattern of soundings with a spacing of the order of the horizontal correlation length scale of the background error covariances of the data assimilation scheme. This sampling is expected to be more efficient than the one-dimensional distribution of the same number of soundings along flight tracks. Finally, the evaluation was performed in a perfect model scenario to focus on forecast errors arising from initial condition errors.

A key result is that the HSVs pointed to the OZO in both cases, whereas the TESVs did so only in the Danish storm case. Given just the two cases, it is too early to conclude that HSVs are better suited for targeting than TESVs. We also found an initial perturbation based on TESVs that results in a good forecast of the French storm. If the initial error is represented by this perturbation, the TESVs identify the relevant part of the initial error rather than the HSVs as additional experiments show. However, the sensitivity of the results to the choice of the initial time singular vector norm indicates that a good estimate of the analysis error covariance metric may be essential for a successful targeting technique.

An interesting issue beyond the scope of this paper is whether the HSVs point to the OZO for the wrong reasons. Recent results by Gilmour *et al.* (2001) imply that nonlinearity may matter already after 1 day for the evolution of typical initial condition errors. They diagnose the nonlinearities from pairs of nonlinear integrations that differ only by the sign of the initial perturbation. In addition to the nonlinear evolution of initially small perturbations in the nonlinear forecast model, the validity of approximations made in the formulation of the tangent-linear model and its adjoint is questionable. Wernli *et al.* (2002) suggest that the French storm can be characterized as a moist Rossby wave in the phase prior to the rapid intensification of the system. Thus, the inclusion of moist processes in the singular vector computation may change the dominating mechanism of error growth and potentially the target regions.

Additional observations in the HSV-targets improved the forecast by a considerable fraction of the improvement obtained with observations in the OZO. The estimated potential for forecast improvement may be too optimistic

if model error was also important, as the evaluation was done in a perfect model scenario. This study did not attempt to determine whether model error or initial condition error was the cause of the forecast failure. In our setting we assumed that forecast error is entirely due to initial condition error.

Given a set of singular vectors it is not clear what the appropriate size of the target region should be as the singular vectors have considerable amplitude even at large distances from the location of their maximum amplitude. The adequate size of the target region and sampling density was estimated through a series of experiments. For the task of improving the 2-day forecast over parts of Europe, it appears that a region of about 3×10^6 km^2 sampled with 10–40 soundings results in a considerable fraction of the forecast improvement obtained with the hemispheric network. This conclusion is based on the subjective evaluation of the sea level pressure maps. In general, the appropriate size and sampling will depend on the specific forecast goal. In addition, the adequate size is linked with the accuracy of the targeting technique. The true sensitive region could be covered eventually by enlarging the target region more and more. Thus, a relatively inaccurate targeting technique may also achieve the forecast goal if the size of the target region is chosen sufficiently large.

For 40 supplementary soundings, the singular vector targeting is superior to the un-targeted RDS as configurations of observing sites are avoided that happen to improve the forecast little. However, on average the RDS performs surprisingly well. This may be due to the fact that some 5–10 of the 40 soundings are very likely to be located in the sensitive region. We expect that the RDS would be considerably worse for a smaller number of soundings, whereas the singular vector targeting still improves the forecast significantly with just 10 soundings.

For the French storm case, the target is very sensitive to the choice of the initial time singular vector norm. Besides this sensitivity there are other factors in the computation which can affect the target region. The sensitivity to the trajectory used for linearization in the singular vector computation has been investigated by recomputing the TESVs and the HSVs using an initial condition taken from truth rather than control. The sensitivity to the trajectory is small. For instance, the medium size target region is modified so little that no more than 5 of 40 sounding locations change for both types of singular vectors.

Our assimilation procedure is different from the operational one in these idealized observing system simulation experiments. The analysis is obtained using the control analysis as background and the supplementary soundings as the only observations. This approach was required to avoid the use of an inhomogeneous set of observations originating from two different systems: the real world and the truth simulation. However, we did not modify the background error covariances to reflect that the error covariances of the control analysis are different from the background error covariance estimates in the assimilation scheme. From a theoretical point, this would be necessary, but we do not expect that the change of the covariances would alter the results of the evaluation much as most observations are taken in poorly observed areas, where the control analysis is mostly determined by the background fields.

Almost all experiments, even those including observational error, showed a noticable forecast improvement. This is at odds with experience from impact studies using field experiment data (e.g. Bergot 2001; Langland *et al.* 1999). Despite the overall positive impact there is a considerable fraction of cases in which the use of supplementary observations increases the forecast error. The perfect model scenario and the efficient two-dimensional sampling of the target regions in our idealized experiments are two factors that may contribute to this discrepancy. Another possible explanation is related to our choice of the control and truth experiments. We investigated cases of forecast failure, that is a large departure of the control experiment from truth at verification time. In an unbiased sample, there would be cases in which the control deviates little from the truth at verification time. We expect that in these cases supplementary observations taken in sensitive regions lead more frequently to a worse forecast due to the presence of observational errors. In the target regions the amplification of analysis perturbations, which arise from observational errors, into forecast errors can be particularly large.

Acknowledgements

We would like to thank Thierry Bergot, François Bouttier, Gérald Desroziers, Mike Fisher, Jim Hansen, Alain Joly, Kamal Puri and Lenny Smith for useful discussions about this work. We thank two anonymous reviewers for their suggestions. Furthermore, ML is grateful to Kamal Puri for initial guidance at ECMWF in the early days of this project and to Erik Andersson and Drasko Vasiljevic who provided valuable help with the assimilation system and processing of observations, respectively. David Richardson is thanked for his help with running the multi-analyses ensemble. Thanks to Carsten Maaß for providing the LaTeX-style file for this memorandum. The funding of this research by the Office of Naval Research under grant N00014–99–1–0755 is acknowledged.

Appendix: Observational error and forecast error

It seems paradoxical that for a fixed error of the background field observational error results in a reduction of the forecast error in a large number of cases. We will show now, that this has to be expected for a linear assimilation procedure and a perfect linear forecast model in the regime of "small" observational errors. Let us write the vector of observed values $\mathbf{y}^{\mathrm{o}}$ as sum of the true values $\mathbf{y}^{\mathrm{t}}$ and an error $\boldsymbol{\varepsilon}$

$$\mathbf{y}^{\mathrm{o}} = \mathbf{y}^{\mathrm{t}} + \boldsymbol{\varepsilon}. \tag{A1}$$

The error is assumed to be unbiased with covariance $\mathcal{E}(\boldsymbol{\varepsilon}\boldsymbol{\varepsilon}^{\mathrm{T}}) = \mathbf{R}$. For the sake of the argument, we assume a linear data assimilation step of the form $\mathbf{x}^{\mathrm{a}} = \mathbf{x}^{\mathrm{b}} + \mathbf{K}(\mathbf{y}^{\mathrm{o}} - H(\mathbf{x}^{\mathrm{b}}))$, where $\mathbf{x}^{\mathrm{a}}, \mathbf{x}^{\mathrm{b}}, H$ and $\mathbf{K}$ denote the analysis state, the background state, the observation operator and the gain matrix, respectively. Then the analysis using the observations with error $\boldsymbol{\varepsilon}$ is equal to

$$\mathbf{x}^{\mathrm{a}} = \overline{\mathbf{x}}^{\mathrm{a}} + \mathbf{K}\boldsymbol{\varepsilon}, \tag{A2}$$

where $\overline{\mathbf{x}}^{\mathrm{a}}$ denotes the analysis obtained with the perfect observations $\mathbf{y}^{\mathrm{t}}$. The analysis $\overline{\mathbf{x}}^{\mathrm{a}}$ is equal to the mean of all analyses obtained for the different realizations of observational error. When the propagator is applied to (A2), we obtain

$$\mathbf{x}^{\mathrm{f}} = \overline{\mathbf{x}}^{\mathrm{f}} + \mathbf{M}\mathbf{K}\boldsymbol{\varepsilon}, \tag{A3}$$

where $\overline{\mathbf{x}}^{\mathrm{f}}$ and $\mathbf{x}^{\mathrm{f}}$ denote the forecast starting from $\overline{\mathbf{x}}^{\mathrm{a}}$ and $\mathbf{x}^{\mathrm{a}}$, respectively.

Thus, the forecast error computed with respect to the true state $\mathbf{x}^{t}$ and measured in a metric $\|\ \|$ coming from an inner product $\langle\ ,\ \rangle$ turns out to be:

$$\|\mathbf{x}^{\mathrm{f}} - \mathbf{x}^{\mathrm{t}}\|^2 = \|\overline{\mathbf{x}}^{\mathrm{f}} - \mathbf{x}^{\mathrm{t}}\|^2 + 2\langle \overline{\mathbf{x}}^{\mathrm{f}} - \mathbf{x}^{\mathrm{t}}, \mathbf{M}\mathbf{K}\boldsymbol{\varepsilon}\rangle + \|\mathbf{M}\mathbf{K}\boldsymbol{\varepsilon}\|^2. \tag{A4}$$

Here, we are interested in the case where the metric is based on total energy in a region defined by a projection operator $\mathbf{P}$: $\langle \mathbf{x}_1, \mathbf{x}_2\rangle = \mathbf{x}_1^{\mathrm{T}}\mathbf{P}^{\mathrm{T}}\mathbf{E}\mathbf{P}\mathbf{x}_2$ and $\|\mathbf{x}\|^2 = \langle \mathbf{x}, \mathbf{x}\rangle$. The second term in (A4) is linear in the error and vanishes when taking the expectation value over all realizations of observational error:

$$\mathcal{E}_{\boldsymbol{\varepsilon}}\left(\|\mathbf{x}^{\mathrm{f}} - \mathbf{x}^{\mathrm{t}}\|^2\right) = \|\overline{\mathbf{x}}^{\mathrm{f}} - \mathbf{x}^{\mathrm{t}}\|^2 + \mathcal{E}_{\boldsymbol{\varepsilon}}\left(\|\mathbf{M}\mathbf{K}\boldsymbol{\varepsilon}\|^2\right) \tag{A5}$$

$$= \|\overline{\mathbf{x}}^{\mathrm{f}} - \mathbf{x}^{\mathrm{t}}\|^2 + \mathrm{trace}\left(\mathbf{E}^{1/2}\mathbf{P}\mathbf{M}\mathbf{K}\mathbf{R}\mathbf{K}^{\mathrm{T}}\mathbf{M}^{\mathrm{T}}\mathbf{P}^{\mathrm{T}}\mathbf{E}^{1/2}\right). \tag{A6}$$

The contribution of the third term in (A4), which is quadratic in $\boldsymbol{\varepsilon}$, will be negligible in the limit of small observational errors. Here, small is to be understood in the sense that the magnitude of the forecast error which

is solely due to observational error $\|\mathbf{MK\varepsilon}\|^2$ is much smaller than the magnitude of the forecast error which is entirely due to the error of the background fields $\|\overline{\mathbf{x}}^{\mathrm{f}} - \mathbf{x}^{\mathrm{t}}\|^2$. In this regime, where the quadratic term in $\boldsymbol{\varepsilon}$ can be neglected, the forecast using the perturbed observations is expected to have a smaller error than the forecast using perfect observations for exactly half of the realizations of observational error.

References

Baker, N. L. and R. Daley, 2000: Observation and background adjoint sensitivity in the adaptive observation-targeting problem. *Q. J. R. Meteorol. Soc.,* **126,** 1431–1454.

Barkmeijer, J., R. Buizza, and T. N. Palmer, 1999: 3d-var Hessian singular vectors and their potential use in the ECMWF Ensemble Prediction System. *Q. J. R. Meteorol. Soc.,* **125,** 2333–2351.

Barkmeijer, J., M. Van Gijzen, and F. Bouttier, 1998: Singular vectors and estimates of the analysis-error covariance metric. *Q. J. R. Meteorol. Soc.,* **124,** 1695–1713.

Bergot, T., 2001: Influence of the assimilation scheme on the efficiency of adaptive observations. *Q. J. R. Meteorol. Soc.,* **127,** 635—660.

Bergot, T., G. Hello, A. Joly, and S. Malardel, 1999: Adaptive observations: A feasibility study. *Mon. Weather Rev.,* **127,** 743–765.

Berliner, L. M., Z.-Q. Lu, and C. Snyder, 1999: Statistical design for adaptive weather observations. *J. Atmos. Sci.,* **56,** 2536–2552.

Bishop, C. H., B. J. Etherton, and S. J. Majumdar, 2001: Adaptive sampling with the ensemble transform Kalman filter. part I: Theoretical aspects. *Mon. Weather Rev.,* **129,** 420–436.

Bishop, C. H. and Z. Toth, 1999: Ensemble transformation and adaptive observations. *J. Atmos. Sci.,* **56,** 1748–1765.

Buizza, R. and A. Montani, 1999: Targeting observations using singular vectors. *J. Atmos. Sci.,* **56,** 2965–2985.

Courtier, P., J. Thépaut, and A. Hollingsworth, 1994: A strategy for operational implementation of 4D-Var using an incremental approach *Q. J. R. Meteorol. Soc.,* **120,** 1367–1387.

Doerenbecher, A. and T. Bergot, 2001: Sensitivity to observations applied to FASTEX cases. *Nonlinear Processes in Geophys.,* **8,** 467–481.

Gelaro, R., R. H. Langland, G. D. Rohaly, and T. E. Rosmond, 1999: An assessment of the singular-vector approach to targeted observing using the FASTEX data set. *Q. J. R. Meteorol. Soc.,* **125,** 3299–3328.

Gilmour, I., L. A. Smith, and R. Buizza, 2001: On the duration of the linear regime: Is 24 hours a long time in weather forecasting? *J. Atmos. Sci.,* **58,** 3525–3539.

Hamill, T. M. and C. Snyder, 2002: Using improved background error covariances from an ensemble Kalman filter for targeted observations. *Mon. Weather Rev., (in press).*

Hansen, J. A. and L. A. Smith, 2000: The role of operational constraints in selecting supplementary observations. *J. Atmos. Sci.,* **57,** 2859–2871.

Langland, R. H. and G. D. Rohaly, 1996: Adjoint-based targeting of observations for FASTEX cyclones. In *Preprints, Seventh Conf. on Mesoscale Processes,* Am. Meteorol. Soc., 369–371.

Langland, R. H., Z. Toth, R. Gelaro, I. Szunyogh, M. A. Shapiro, S. J. Majumdar, R. E. Morss, G. D. Rohaly, C. Velden, N. Bond, and C. H. Bishop, 1999: The North Pacific experiment (NORPEX-98): Targeted observations for improved North American weather forecasts. *Bull. Am. Meteorol. Soc.,* **80,** 1363–1384.

Lorenz, E. N. and K. A. Emanuel, 1998: Optimal sites for supplementary weather observations: Simulation with a small model. *J. Atmos. Sci.,* **55,** 399–414.

Montani, A. and A. J. Thorpe and R. Buizza and P. Unden, 1999: Forecast skill of the ECMWF model using targeted observations during FASTEX. *Q. J. R. Meteorol. Soc.,* **125,** 3219–3240.

Morss, R. E., K. A. Emanuel, and C. Snyder, 2001: Idealized adaptive observation strategies for improving numerical weather prediction. *J. Atmos. Sci.,* **58,** 210–234.

Palmer, T. N., R. Gelaro, J. Barkmeijer, and R. Buizza, 1998: Singular vectors, metrics, and adaptive observations. *J. Atmos. Sci.,* **55,** 633–653.

Pearce, R., D. Lloyd, and D. McConnell, 2001: The post-Christmas 'French' storms of 1999. *Weather,* **56,** 81–91.

Pu, Z.-X., E. Kalnay, J. Sela, and I. Szunyogh, 1997: Sensitivity of forecast error to initial conditions with a quasi-inverse linear method. *Mon. Weather Rev.,* **125,** 2479–2503.

Rabier, F. and P. Courtier, 1992: Four-dimensional assimilation in the presence of baroclinic instability. *Q. J. R. Meteorol. Soc.,* **118,** 649–672.

Reynolds, C. A., R. Gelaro, and T. N. Palmer, 2000: Examination of targeting methods in a simplified setting. *Tellus,* **52 A,** 391–411.

Richardson, D. S., 2001: Ensembles using multiple models and analyses. *Q. J. R. Meteorol. Soc.,* **127,** 1847–1864.

Snyder, C., 1996: Summary of an informal workshop on adaptive observations and FASTEX. *Bull. Am. Meteorol. Soc.,* **77,** 953–961.

Szunyogh, I., Z. Toth, R. E. Morss, S. J. Majumdar, B. J. Etherton, and C. H. Bishop, 2000: The effect of targeted dropsonde observations during the 1999 winter storm reconnaissance program. *Mon. Weather Rev.,* **128,** 3520–3537.

Ulbrich, U., A. H. Fink, M. Klawa, and J. G. Pinto, 2001: Three extreme storms over Europe in December 1999. *Weather,* **56,** 70–80.

Wernli, H., S. Dirren, M. A. Liniger, and M. Zillig, 2002: Dynamical aspects of the life-cycle of the winter storm 'Lothar' (24-26 December 1999). *Q. J. R. Meteorol. Soc., (accepted).*